SYNTHESIS AND CHARACTERIZATION OF LOW AND NEGATIVE THERMAL EXPANSTION MATERIALS

A Thesis
Presented to
The Academic Faculty

by

Mehmet Nuri Kütükçü

In Partial Fulfillment
of the Requirements for the Degree
Masters of Science in the
School of Chemistry and Biochemistry

Georgia Institute of Technology
December 2005

SYNTHESIS AND CHARACTERIZATION OF LOW AND NEGATIVE THERMAL EXPANSION MATERIALS

Approved by:

Dr. Angus P. Wilkinson, Advisor
School of Chemistry and Biochemistry
Georgia Institute of Technology

Dr. E. Kent Barefield
School of Chemistry and Biochemistry
Georgia Institute of Technology

Dr. Z. John Zhang
School of Chemistry and Biochemistry
Georgia Institute of Technology

Date Approved: November 22, 2005

Dedicated to;

My Mother Sekinet Kütükçü

And

My Father Alaattin Kütükçü

Annem Sekinet Kütükçü

ve

Babam Alaattin Kütükçü'ye

ACKNOWLEDGEMENTS

First and foremost, I would like to thank my advisor Prof. Angus P. Wilkinson for his support and guidance which made this work possible. I also want to thank to Prof. E. Kent Barefield and Prof. Z. John Zhang, for their valuable time and comments throughout my time at GaTech and as well as for being on my reading committee.

In the course of this work there have been many people kindly assisted me with their knowledge and experience with various techniques and equipment. I would like to thank to Dr. Andrew Payzant for his assistance with high temperature powder X-ray diffraction data collection and analyzing the data at the High Temperature Materials Laboratory at Oak Ridge National Laboratory. I would also like to thank to Dr. Peter Chupas for his assistance with the synchrotron experiments at the Advanced Photon Source at Argonne National Laboratory. SEM and EDX studies were performed at Georgia Institute of Technology Microscopy center and the assistance and training by Ms. Yolande Berta is appreciated. Another thank you goes to Dr. Johannes Leisen for his help with ^{69}Ga-NMR which could not make it into this thesis. I want to thank all the other people, whose name is not listed here, for their assistance with many laboratory equipment and valuable time.

The past and the present members of Wilkinson Group whom I loved to work with are also given thanks for their friendship and help. I especially want to thank Mehmet Çetinkol who was always with me from start to the end not only as a colleague but also as my best friend. I want to thank Kathy White for her help and tasteful conversations. I want to thank Dr. Andrew C. Jupe for his help in data analysis and any

type of problems with computers. I also want to thank to Dr. Tamas Varga for his support and friendship.

Finally, I want to thank to my friends, so called “Turkish Mafia”, for their support on my professional decisions and unforgettable times together at GaTech.

TABLE OF CONTENTS

LIST OF TABLES

LIST OF FIGURES

SUMMARY

The preparation and thermophysical properties of some In(I), Ga(I) and Ag(I) substituted NZP type materials were explored. Many compositions with the NZP framework show low and negative thermal expansion.

Chapter 3 describes the thermophysical characterization of the previously reported material; $GaZr_2(PO_4)_3$. The material transforms from one NZP related phase into another NZP type phase due to oxidation under air above 300^{o}C. In addition, it exhibits hysteresis under an inert atmosphere; the cell parameters are different on heating and cooling cycles for a given temperature. In Chapter 4, the synthesis, and characterization of a new material, $InZr_2(PO_4)_3$, is outlined. It crystallizes in space group R -3 c. Like $GaZr_2(PO_4)_3$, it oxidizes above 300^{o}C under air and exhibits hysteresis in its cell constants on heating under inert atmosphere. In Chapter 5, the synthesis of $Ag[Ti_xZr_{2-x}](PO_4)_3$ solid solution compositions, their ion exchange characteristics with Ga(I) and their thermophysical properties are described. Thermal expansion anisotropy (the difference between α_a and α_c) of the solid solutions decreases as the bigger ion, Zr^{4+}, is substituted by the smaller one, Ti^{4+}. Initially, it was expected that the ion exchange ratio of Ga(I) to Ag(I) in the solid solutions would follow a smooth trend. However, while above x = 1.25 there is zero Ga(I) exchange, below x = 1 material ion exchanges. Finally, in Chapter 6, thermal expansion characteristics of $GaZr_2(PO_4)_3$, $InZr_2(PO_4)_3$ and $AgZr_2(PO_4)_3$ are compared with $MZr_2(PO_4)_3$ (M = Li, Na, K, Rb, Cs). Ionic radii for Ga(I) and In(I) in a six coordinate oxygen environment were proposed.

CHAPTER 1

INTRODUCTION

1.1 Thermal Expansion

One of the very important properties of materials for many technological and practical applications is thermal expansion. Controlling the thermal expansion property of the materials is needed for a wide variety of applications like cookware for oven to freezer, electronic devices, dental applications, zero-expansion heat sinks, engine components, spark plugs, catalyst supports, high performance optical mirror substrates, etc. Investigation of the structural mechanisms helps to control the thermal expansion behavior of materials

Thermal expansion of a material can be either intrinsic or extrinsic. Intrinsic thermal expansion is based on the changes of crystallographic unit cell axes with respect to temperature and it is measured with X-ray diffraction or neutron diffraction. Intrinsic thermal expansion can be isotropic or anisotropic. Isotropic materials show the same magnitude of thermal expansion in all dimensions of the unit cell and they are cubic or amorphous. On the other hand; anisotropic materials have different magnitude of thermal expansion along the different unit cell axes. When a single phase ceramic made of an anisotropic material is heated, micro cracks may from, because of the different expansion behavior of the unit cell axes. If the thermal expansion of a ceramic body is measured directly, these micro cracks affect the overall thermal expansion of the ceramic body on

repeated heat treatments. Therefore, it is very hard to reproduce the same thermal expansion for the ceramic. Materials with a high thermal expansion coefficient also show micro cracking during rapid heating or cooling. In addition, micro cracks lower the mechanical strength of the material which is undesirable. Therefore, isotropic materials with low or near-zero CTE are very important for applications.

Almost all of the materials expand upon heating as the interatomic distance between two atoms increases. If the interatomic potential function is assumed to be harmonic, when temperature increases from T1 to T2 (T2>T1), the average distance between two atoms, R, will not change (Figure 1.1).

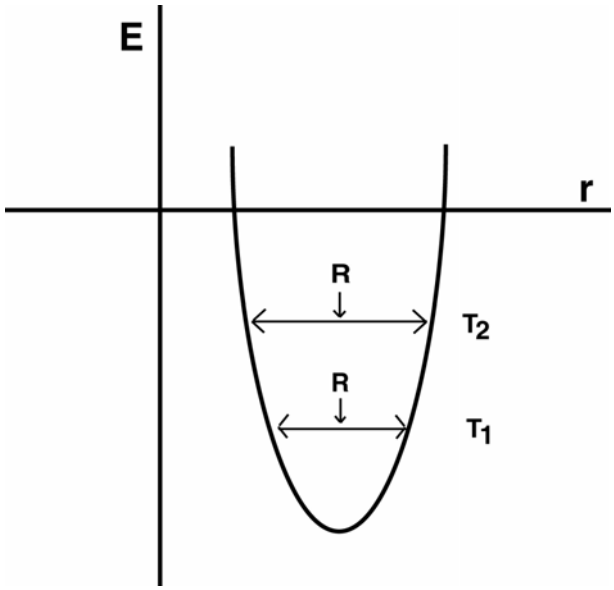

Figure 1.1: Potential energy as a function of interatomic distance R for a harmonic system. Average R does not change due to temperature change.

However, in the real world, the interatomic potential function is anharmonic (Figure 1.2). Therefore, as the temperature increases from T1 to T2 (T2>T1), average distance between two atoms increases from R1 to R2 (R2>R1), which causes thermal

expansion. As the bond between two atoms gets stronger, potential function becomes more symmetric and the vibrations become more harmonic. Furthermore, if the bond is strong enough, thermal expansion may even be undetectable. In fact, a common strategy to synthesize low or negative thermal expansion materials is to choose strongly bonded structures.

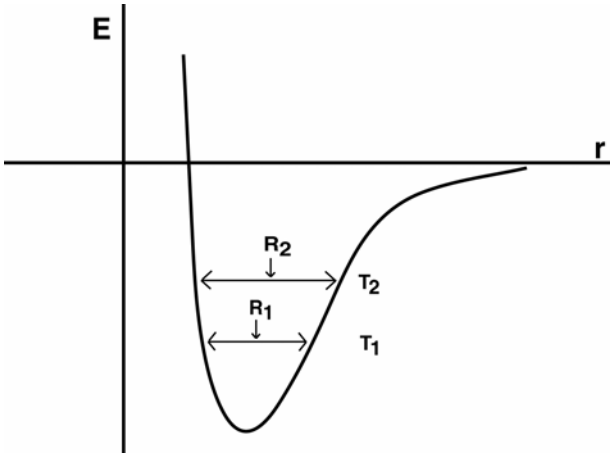

Figure 1.2: Potential energy as a function of interatomic distance r for an anharmonic system. Average R increases due to increasing temperature.

The linear and volumetric coefficients of thermal expansion are defined as;

$$\alpha = \frac{1}{l}\left(\frac{dl}{dT}\right)_p \qquad \alpha_v = \frac{1}{V}\left(\frac{dV}{dT}\right)_p$$

where *l* is the length and *V* is the volume and *dl* and *dV* are the changes in the length and the volume of the solid due to temperature change *dT*, respectively. For a crystal structure, *dl* is taken as the change in a crystallographic axis. Therefore, α_{ave} of the cubic materials are same with the linear coefficient of thermal expansion in one crystallographic axis. However, as the crystallographic axes are different for non cubic

materials, α_{ave} will be the average of all linear coefficients of thermal expansions in all axes. For instance, for a rhombohedral lattice the average linear expansion coefficient will be;

$$\alpha_{ave} = (2\alpha_a + \alpha_c)/3$$

Materials can be arbitrarily classified into three groups depending on their absolute value of coefficient of thermal expansion[1]:

High Expansion Group: $\alpha > 8 \times 10^{-6}\ K^{-1}$

Intermediate Group: $2 < \alpha < 8 \times 10^{-6}\ K^{-1}$

Low Expansion Group: $\alpha < 2 \times 10^{-6}\ K^{-1}$

From the technological point of view, materials in the last group are the most important ones. Before the 1950s, three families of low thermal expansion materials; zircon ($ZrSiO_4$), cordierite ($Mg_2Al_4Si_5O_{18}$) and silica glass (SiO_2), were known. In 1948, Hummel reported a new family of lithium aluminum silicates, *β*-eucryptite ($LiAlSiO_4$) and *β*-spodumene ($LiAlSi_2O_6$), which show negative and low thermal expansion, respectively.[2, 3] However, after Hummel's report many attempts to substitute the ion in the stuffing site to improve the properties failed and except for the spodumene-cordierite[4] system, no technologically important solid solutions could be synthesized. This family dominated the low and negative thermal expansion industry for almost forty years and is used in many applications. In 1979, Boilot[5] reported that in the $Na_{1+x}Zr_2P_{3-x}Si_xO_{12}$ system, known as NZP, thermal expansion of the material changes from strongly positive to near zero with decreasing x. Further research showed that unlike the lithium aluminum silicate system, the NZP structure allows a huge variety of ion substitutions not only to the vacancies in the structure but also to the rigid framework.[6] After Boilot, a variety of

solid solutions with the NZP structure were synthesized and some of them are being commercially used today.

Some of the important low thermal expansion materials and their average coefficient of thermal expansions are listed in Table 1.1.

Table 1.1 Coefficient of thermal expansion of some low CTE materials.[1]

Material	CTE ($^oC^{-1}$ x 10^6)	Temperature Range(^oC)
$ZrSiO_4$	0 ± 0,10	0-50
$Mg_2Al_4Si_5O_{18}$	1.4	25-800
SiO_2 glasses	0.5	25-1000
SiO_2- TiO_2 glasses	0.05-(-0.03)	25-800
β-eucryptite ($LiAlSiO_4$)	-6.2	25-1000
β-spodumene ($LiAlSi_2O_6$)	0.9	25-1000
$NaZr_2(PO_4)_3$	-0.4	25-1000

1.2 Negative Thermal Expansion

Negative thermal expansion (NTE) is not an expected property for materials because of the reason explained in section 1.1. However, it is potentially important for many applications. Materials showing NTE can be used in composites to adjust the overall thermal expansion to a desirable value. In many applications, there is a need for materials that have exact matching coefficient of thermal expansion to the other device parts with desired other properties like adhesion or elastic moduli. In most of the cases this can only be achieved by using composites. Therefore, study of this unexpected property is not just scientifically interesting but also important for many practical applications.

NTE is seen in different type of substances. One interesting and well known example of these substances is water, which increases in density between 0 to 4 ^oC. There

are many other substances showing NTE and mechanisms of it are due to many different affects. However, for the purposes of the research, only the mechanism of NTE in solid oxides will be the focus of this introduction.

Solid oxides have been investigated for decades because of their low and negative thermal expansion, high temperature stability, resistance to chemical reactions, ionic conductivity, etc. NTE in solid oxides can not be explained by just interatomic or simple structural models. In order to understand the mechanisms, unique features of crystal structures have to be studied. In addition, there are some guidelines to investigate new NTE materials:

- Structure should consist of strongly bonded polyhedra to minimize bond length enlargement due to temperature increase. For instance, thermal expansion of P-O and Zr-O bonds are so small that they are usually ignored in the calculations. In addition, $NaZr_2(PO_4)_3$ has a rigid three dimensional framework of corner shared ZrO_6 octahedra and PO_4 tetrahedra and thermal expansion contribution of the framework atoms to the overall thermal expansion is very small.[7]
- Material should have an open and flexible structure to accommodate contraction.
- Structure may have ferroelectric or ferromagnetic microdomains which may compensate the dimensional changes caused by thermal energy with their distribution.[1] Classic example is the alloy invar.

Since the discovery of solid oxides showing NTE, four different mechanisms of negative thermal expansion have been identified.[8]

Some AMO_3 type solid oxides with perovskite structure show NTE just below their tetragonal to cubic phase transition which can also be called symmetry related

NTE[7]. These solids are tetragonal at low temperatures and cubic at higher temperatures. In addition, when the structure is tetragonal, it consists of highly distorted AO_{12} polyhedra and MO_6 octahedra. As temperature increases close to solid oxides phase transition, AO_{12} and MO_6 become more regular. It is well known that average metal-oxygen bond length decreases as the polyhedra become more regular[9]. This change from highly distorted to regular polyhedra and octahedra causes the material to contract along the c direction and expand along a and b directions giving an overall volume negative thermal expansion. This behavior can be explained by the fact that anion-anion repulsions are minimized as the polyhedra become more regular. After the material becomes cubic, it shows normal thermal expansion. $BaTiO_3$ and $PbTiO_3$ are good examples of materials showing this NTE mechanism.[8]

Materials like cordierite ($Mg_2Al_2Si_5O_{18}$), β-eucryptite ($LiAlSiO_4$) and some materials with NZP ($NaZr_2(PO_4)_3$) like structure show thermal contraction because of the expansion in certain M-O (M = Metal) bonds. They have rigid three dimensional frameworks and expansion along one or two crystallographic axes is coupled with contraction along the other axes. All of these materials have hexagonal structure and their thermal expansion behavior is highly anisotropic. Cordierite and *β*-eucryptite expand along a and b axes and contract along the c axis (Figure 1.3). On the other hand, NZP structure does the opposite, contract along a and b axes and expand along c axis (Figure 1.4).

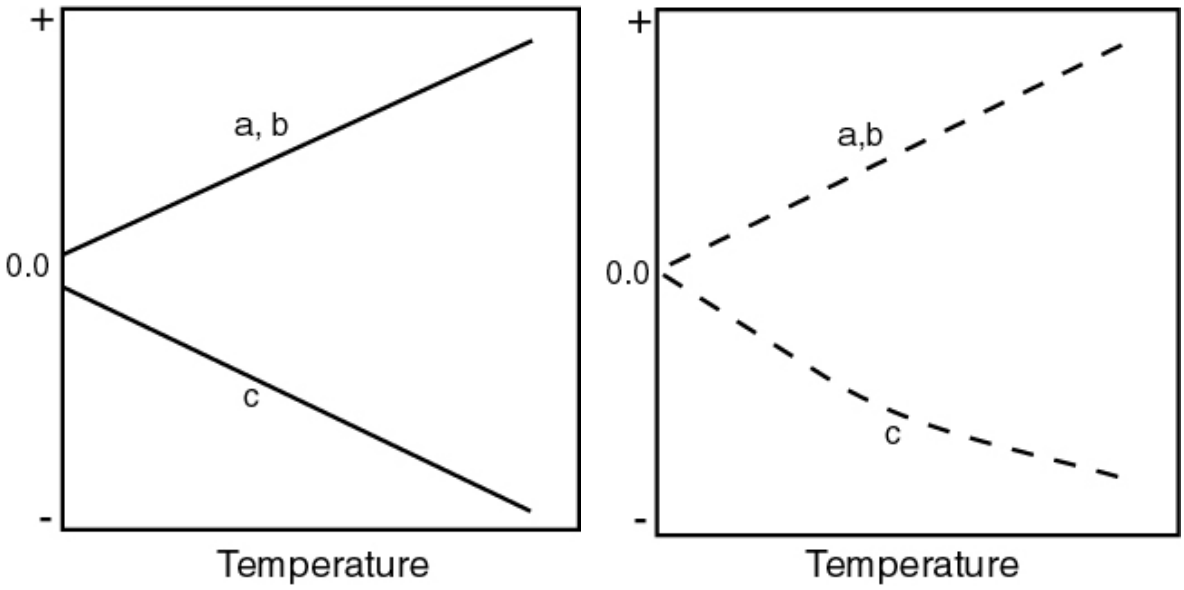

Figure 1.3: Cell parameters of (Left) Cordierite, (Right) β-eucryptite as a function of temperature. Expansion along a and c crystallographic axes is coupled with the contraction along c axis.

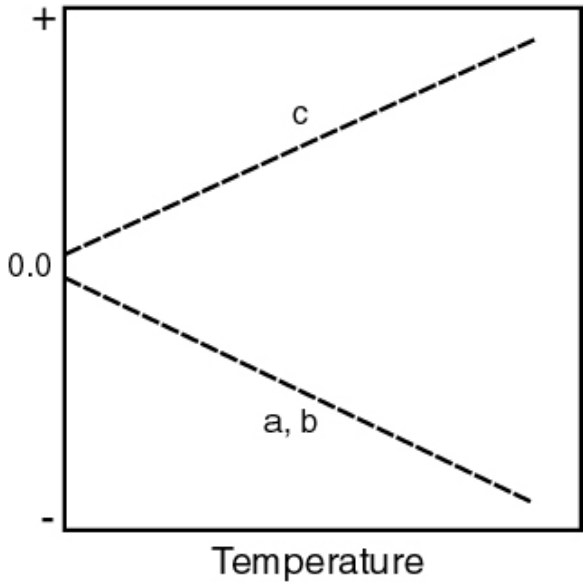

Figure 1.4: Cell parameters of NZP family as a function of temperature. Expansion along c crystallographic axis is coupled with the contraction along a and b axes.

Si-O, P-O, Al-O and Zr-O bonds are very strong and their thermal expansion is negligible. However, Mg-O, Li-O and Na-O bonds are weaker and they show significant thermal expansion. In cordierite, expansion of Mg-O bonds results in thermal expansion of two dimensions because of the structural arrangements. As two dimensions expand, the third one contracts pulling the expanding sheets closer. Using this structural information thermal expansion of cordierite can be quantitatively modeled. Figure 1.5 is a representation of the cordierite structure in which a is one side of the expanding sheet and c is the distance between the expanding sheets.[10] However, in order to calculate the thermal expansion of β-eucryptite ($LiAlSiO_4$) and NZP family other mechanisms have to be included.

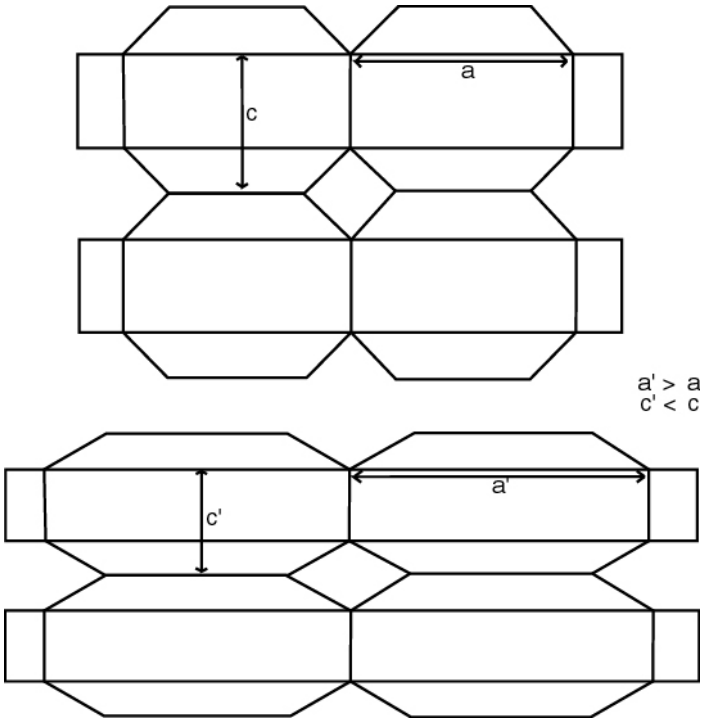

Figure 1.5: Representation of the cordierite structure. a is one side of the expanding sheet and c is the distance between the expanding sheets. As the sheets through a expands, they are pulled together (c^1>c).

Some materials show NTE because of interstitial cation movement through the network as a function of temperature. This mechanism is significant for ionic conductor solids like β-eucryptite ($LiAlSiO_4$) and the NZP family. Calculations of the Li^+ ion movement in β-eucryptite from tetrahedral sites to octahedral sites explains the observed negative thermal expansion of the material. In addition, the thermal expansion of some NZP family members is also strongly dependent on cation movements.[8]

The last mechanism of NTE in solid oxides is the traverse motion of oxygen between M-O-M linkages. If the M-O-M angle is close to 180^o and the M-O bond is strong, primary vibration of oxygen will be perpendicular to the line between the metals. Furthermore, as the temperature increases, average primary vibration will increase and the metals will be pulled together causing a decrease in the average metal to metal distance (Figure 1.6). This effect can be seen in any structure. In fact, it is the accepted explanation of NTE in amorphous SiO_2 and many crystalline forms of SiO_2 above 1000 ^oC.[11] In the case of Cu_2O the effect is reversed. The primary vibration of copper is perpendicular to the line between oxygen atoms pulling them together, causing NTE.

There are some issues of getting NTE in a material with this mechanism. In order to get NTE, the material should have an open framework, composed of rigid polyhedra and the oxygen atoms should be in two-fold coordination. The rigid polyhedra should tilt forth and back to give the traverse thermal motion of oxygen. This mechanism is one of the proposed mechanisms to explain the isotropic NTE in ZrW_2O_8.

Some of the important negative thermal expansion materials and their average coefficient of thermal expansions are listed in Table 1.2.

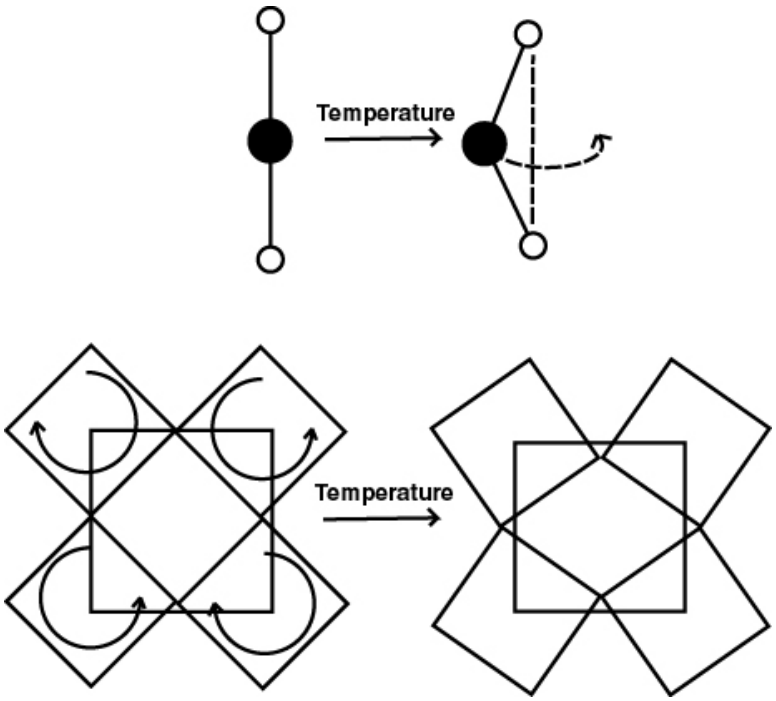

Figure 1.6: Representation of the traverse motion of M-O-M resulting negative thermal expansion. Adapted from Evans et al.[12]

Table 1.2 Coefficient of thermal expansion of some NTE materials.

Material	**Symmetry**	**CTE [10^{-6}/ K]**	**Temperature [K]**
$K_5Zr(PO_4)_3$	Hexagonal	-0.5	293-1023[13]
$KZr_2(PO_4)_3$	Hexagonal	-1.7	293-1023[13]
Glass 90.55 SiO_2 / 9.45 TiO_2		-1.8	278-308[14]
$Sc_2W_3O_{12}$	Orthorhombic	-2.2	50-1073[12]
$PbTiO_3$	Tetragonal	-3.3	303-673[15]
$NbOPO_4$	Tetragonal	-3.7	673-973[16]
Si-Zeolite Y	Cubic	-4.2	25-570[17]
$Y_2W_3O_{12}$	Orthorhombic	-4.2	15-1373[18]
$ZrMo_2O_8$	Cubic	-5	11-573[19]
$Lu_2W_3O_{12}$	Orthorhombic	-6.8	400-900[20]
ZrV_2O_7	Cubic	-7.1	400-500[15]
ZrW_2O_8	Cubic	-8.7	20-430[21]
$AlPO_4$-17	Hexagonal	-11.7	18-300[22]
$Zn(CN)_2$	Cubic	-18.1	14-305[23]

For the purposes of the research presented in this thesis, detailed structural information of NZP family will be explained in the next section.

1.2.1 NZP Family

The structure of $NaZr_2(PO_4)_3$ was first reported in 1968 to be rhombohedral with the space group R-3c.[24] The importance of the structure lies in the three dimensional rigid framework which is stable and flexible, and the possibility of preparing hundreds of different compositions. The framework is composed of ZrO_6 octahedra and PO_4 tetrahedra that share corners through strong P-O-Zr bonds. In addition, counter ion Na^{+1} is located in the specific M1 site inside the framework. This compound is a prototype for a broad family of compounds called "NZP".

General formula for the NZP family is $M(I)_{0\rightarrow1}\ M(II)_{0\rightarrow3}M(III)_{0\rightarrow1}A_{2n}(XO_4)_{3n}$ in which $[A_{2n}(XO_4)_{3n}]^{m-}$ represents the rigid framework and M(I), M(II) and M(III) represent the three distinct empty sites in the framework (Figure 1.7). Depending on the composition of the material the symmetry may lower from R-3 c to R-3, C2/c, Cc, etc.[6, 25]

In the compounds with the highest symmetry R-3 c, the M(I) site has -3 symmetry and the coordination number is 6. It lies on the c axis and generally this site is fully or partially occupied. The M(II) site has 2 symmetry and the coordination number is 14. It lies between the columns and is connected to the M(I) site allowing ionic conductivity. Furthermore, as the M(II) site is very big, in some cases two cations may fit into the site.[6] The M(III) site is a distorted trigonal prism and has 32 symmetry. It can only accommodate very small ions and in most cases it is empty.

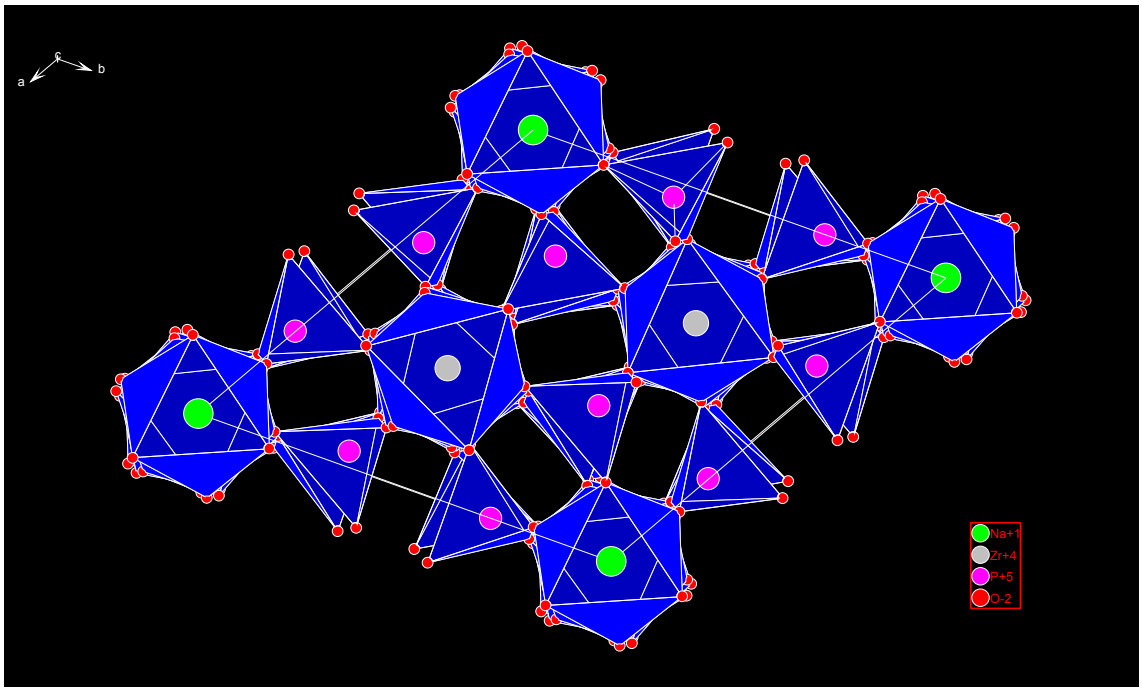

A

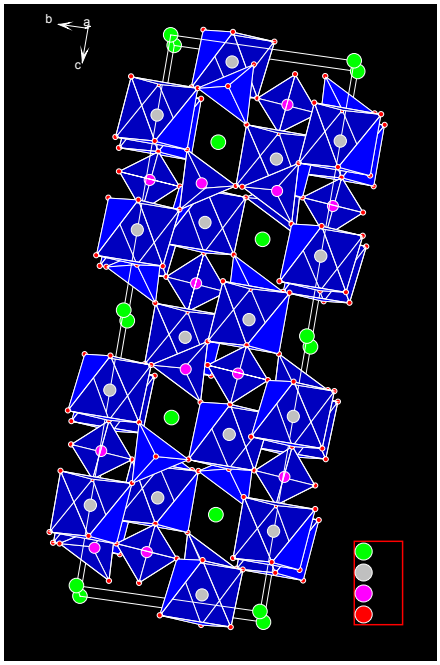

B

Figure 1.7: Structure of $NaZr_2(PO_4)_3$ along the c axis (A) and along the a axis (B). Channels through c axis are connected forming a three dimensional network. The M(I) site is located on the c axis.

M, A and X can be substituted with many different elements forming hundreds of different compositions.[26] M can be substituted with H^{+}, Li^{+}, Na^{+}, K^{+}, Rb^{+}, Cs^{+}, Cu^{+}, Ag^{+}, Ga^{+}, Tl^{+}, NH^{+}, Mg^{2+}, Ca^{2+}, Sr^{2+}, Ba^{2+}, Mn^{2+}, Co^{2+}, Ni^{2+}, Cu^{2+}, Zn^{2+}, Cd^{2+}, Hg^{2+}, Fe^{3+}, Ln^{3+}, Bi^{3+}, Zr^{4+}, $Hf4^{4+}$, A can be substituted with Nb^{5+}, Ta^{5+}, V^{5+}, Sb^{5+}, Ti^{4+},Zr^{4+}, Hf^{4+}, Ge^{4+},Sn^{4+},Mo^{4+}, U^{4+}, Np^{4+}, Pu^{4+}, Nb^{4+}, Sc^{3+}, Y^{3+}, Ln^{3+}, V^{3+}, Cr^{3+}, Fe^{3+}, Co^{3+}, Al^{3+}, Ga^{3+}, In^{3+}, Ti^{3+}, Mg^{2+}, Mn^{2+}, Cu^{2+}, Co^{2+}, Ni^{2+}, Zn^{2+}, Na^{+}, K^{+}, and L can be substituted with As^{5+}, Si^{4+}, Ge^{4+}, S^{6+}, Mo^{6+}, Al^{3+}. Different compositions give several different properties to the structure like ionic conductivity, low and negative thermal expansion, ability to immobilize radioactive nuclides, ferroelectricity and catalytic activity. Substituting M site ions can be done at relatively low temperatures, around 300 ^{o}C, and the framework ions, A and X, can be done at higher temperatures, more than 800 ^{o}C. As the oxidation state of A and X gets higher the framework becomes stronger and the number of different substitutions to the M site increases.

Inside of the framework, $[A_{2n}(XO_4)_{3n}]^{m-}$, M^{1+} counter ions fully occupy the M(I) vacancy, which is located on the c axis, between two ZrO_6 octahedra. In addition, as the M^{+1} ion gets bigger, the c axis expands and PO_4 tetrahedra distort. Distortion of PO_4 tetrahedra increases the O-P-O angle through c axis, which shortens the a axis.

In this research presented, univalent Ga and In ion substitution characteristics to the M(I) site and the effect of ns^2 valence pair electrons to the thermal expansion behavior of the NZP structure are investigated. Univalent Ga and In are more polarizable than other ions of similar size and charge because of their ns^2 valence electrons. In addition, these electrons may cause the displacement of the atoms from the center of the polyhedra which is observed in materials with enhanced ferroelectric properties.

1.3. References

1. Roy, R.; Agrawal, D. K.; McKinstry, H. A., Very Low Thermal Expansion Coefficient Materials. *Annual Review of Materials Science* **1989,** 19, 59-81.

2. Hummel, F. A., Thermal expansion properties of natural lithia minerals. *Foote Prints* **1948,** 20, (2), 3-11.

3. Hummel, F. A., Thermal Expansion Properties of Some Synthetic Lithia Minerals. *Journal of the American Ceramic Society* **1951,** 34, 235-239.

4. Karkhanavala, M. D.; Hummel, F. A., The Polymorphism of Cordierite. *Journal of the American Ceramic Society* **1953,** 36, (12), 389-392.

5. Boilot, J. P.; Salanie, J. P.; Desplanches, G.; Potier, D. L., Phase Transformation in $Na_{1+x}Si_xZr_2P_{3-x}O_{12}$ Compounds. *Materials Research Bulletin* **1979,** 14, 1469-1477.

6. Alamo, J., Chemistry and properties of solids with the [NZP] skeleton. *Solid State Ionics* **1993,** 63-65, 547-561.

7. Sleight, A. W., Compounds that Contract on Heating. *Inorganic Chemistry* **1998,** 37, 2854-2860.

8. Sleight, A. W., Negative thermal expansion materials. *Current Opinion in Solid State and Materials Science* **1998,** 3, 128-131.

9. Brown, I. D.; Shannon, R. D., Empirical bond-strength-bond-length curves for oxides. *Acta Crystallographica Section A* **1973,** 29, (3), 266-282.

10. Sleight, A. W., Thermal Contraction. *Endeavour* **1995,** 19, 64-68.

11. White, G. K., Solids: thermal expansion and contraction. *Contemporary Physics* **1993,** 34, 193-204.

12. Evans, J. S. O.; Mary, T. A.; Sleight, A. W., Negative thermal expansion materials. *Physica. B* **1998,** 241-243, 311-316.

13. Orlova, A. I.; Kemenov, D. V.; Pet'kov, V. I.; Zharinova, M. V.; Kazantsev, G. N.; Samoilov, S. G.; Kurazhkovskaya, V. S., Ultralow and negative thermal expansion in zirconium phosphate ceramics. *High Temperatures-High Pressures* **2002,** 34, (3), 315-322.

14. Schultz, P. C.; Smyth, H. T., Ultra-low-expansion glasses and their structure in the SiO2-TiO2 System. *Amorphous Materials*, ed.; Douglas, R. W.; Ellis, B., Wiley Interscience, London, New York: 1972; p 453-461.

15. Evans, J. S. O., Negative Thermal Expansion Materials. *Journal of the Chemical Society Dalton Transactions* **1999**, 3317-3326.

16. Amos, T. G.; Sleight, A. W., Nagative Thermal Expansion in Orthorhombic $NbOPO_4$. *Journal of Solid State Chemistry* **2001,** 160, 230-238.

17. Attfield, M. P.; Sleight, J. P., Strong negative thermal expansion in siliceous Faujasite. *Chemical Communications* **1998**, 601-602.

18. Forster, P. M.; Sleight, A. W., Negative thermal expansion in $Y_2W_3O_{12}$. *International Journal of Inorganic Materials* **1999,** 1, 123-127.

19. Lind, C.; Wilkinson, A. P.; Hu, Z.; Short, S.; Jorgensen, J. D., Synthesis and Properties of the Negative Thermal Expansion Material Cubic Zirconium Molybdate. *Chemistry of Materials* **1998,** 10, 2335-2337.

20. Forster, P. M.; Yokochi, A.; Sleight, A. W., Enhanced Negative Thermal Expansion in $Lu_2W_3O_{12}$. *Journal of Solid State Chemistry* **1998,** 140, 157-158.

21. Sleight, A. W., Isotropic Negative Thermal Expansion. *Annual Review of Materials Science* **1998,** 28, 29-43.

22. Attfield, M. P.; Sleight, A. W., Exceptional Negative Thermal Expansion in $AlPO_4$-17. *Chemistry of Materials* **1998,** 10, 2013-2019.

23. Williams, D. J.; Partin, D. E.; Lincoln, F. J.; Kouvetakis, J.; O'Keeffe, M., The disordered crystal structures of Zn(CN)(2) and Ga(CN)(3). *Journal of Solid State Chemistry* **1997,** 134, (1), 164-169.

24. Hagman, L. O.; Kierkega.P, Crystal Structure of NaMe2(Po4)3 - Me4 =Ge Ti Zr. *Acta Chemica Scandinavica* **1968,** 22, (6), 1822-&.

25. Ingalls, R.; Garcia, G. A.; Stern, E. A., X-Ray Absorption at High Pressure. *Physical Review Letters* **1978,** 40, 334-336.

26. Pet'kov, V. I.; Orlova, A. I., Crystal-chemical approach to predicting the thermal expansion of compounds in the NZP family. *Inorganic Materials* **2003,** 39, (10), 1013-1023.

CHAPTER 2

INSTRUMENTAL METHODS

2.1 Laboratory X-ray diffraction

Laboratory x-ray diffraction has been used extensively in this research. In the following paragraphs an overview of the analysis methods and the evaluation software in addition to the specifications of the instruments will be given.

2.1.1 Powder x-ray diffraction instruments

Scintag X1 diffractometer with a Cu tube and a Peltier-cooled solid state detector was used extensively in this research.

Some of the high temperature in-situ powder X-ray diffraction data was collected with a Philips X'Pert PRO MPD X-ray powder diffractometer equipped with a scintillation point detector and an Anton-Paar HTK1200 high temperature stage in the X-ray Analysis Group, Materials Science and Engineering, Georgia Institute of Technology. A parallel beam configuration (PreFIX optics) with 0.04 radian soller slits and 10 mm fixed mask on the incident beam side and 0.04 radian soller slits and 0.09^{o} parallel plate collimator on the diffracted beam side was used during the experiments.

The rest of the high temperature X-ray data was collected at the High Temperature Materials Laboratory, Oak ridge National Laboratory using a Philips X'Pert PRO MPD X-ray powder diffractometer equipped with an X'Celerator "Real-Time Multiple Strip" detector and an Anton-Paar XRK900 high-temperature stage (Figure 2.1). Furthermore, 0.04 radians soller slit, 10 mm fixed mask, programmable divergence slit

and 0.04 radians soller slit, nickel foil, a programmable anti scatter slit were used on the incident and diffracted beam sides, respectively.

Figure 2.1**:** Left; X'Celerator "Real-Time Multiple Strip" detector and the Anton-Paar HTK 1200 high-temperature stage, Right; Sample holder.

2.1.2 Powder pattern analysis with the program JADE

The program JADE[1] was used to visualize the diffraction patterns and identify the phases present in the samples. Variable temperature experiments presented in this thesis are plotted using this program.

2.1.3 Analysis of diffraction data: Rietveld refinement

The General Structure Analysis System (GSAS)[2] program with the EXPGUI[3] graphical user interface was used for Rietveld analysis of the X-ray powder diffraction data. High quality powder diffraction data in combination with the Rietveld method allows refinement of a structural model (atomic coordinates, site occupancies and atomic displacement parameters) as well as profile parameters (lattice constants, peak shape, sample height, instrument parameters, background). Changes in unit cell size, in bond lengths and angles (e.g. due to thermal expansion) and other structural information can be

extracted. In this research, all the powder patterns were fitted to a structural model and extracted parameters will be presented. In addition, changes in the structural parameters of the compounds with temperature will be compared.

2.2 Synchrotron X-ray diffraction

Synchrotron radiation is in many cases preferred over laboratory x-ray sources for a wide range of structural investigations. Synchrotrons are powerful radiation sources; their intensity is up to 10^{10} times larger than that of laboratory x-ray tubes. Synchrotron radiation is produced when a charge (electron or positron) moving at relativistic speeds follows a curved trajectory. This trajectory is an enormous vacuum ring in which the electrons are radially accelerated by bending magnets, and therefore emit electromagnetic radiation. In addition, its much higher intensity makes the observation of very weak signals possible (Figure 2.2).

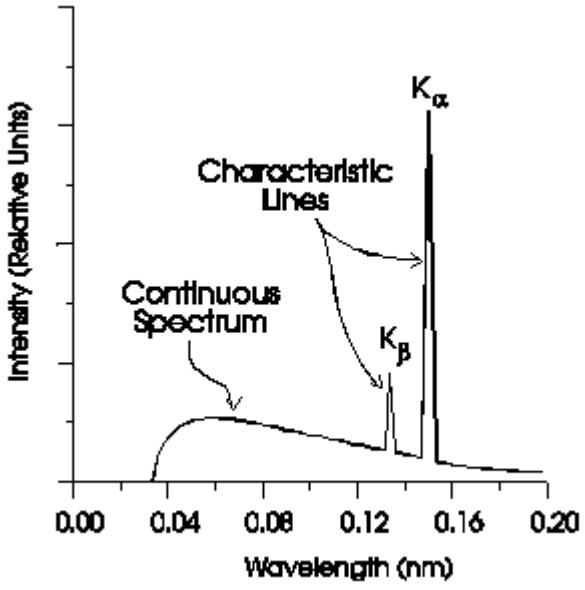

A

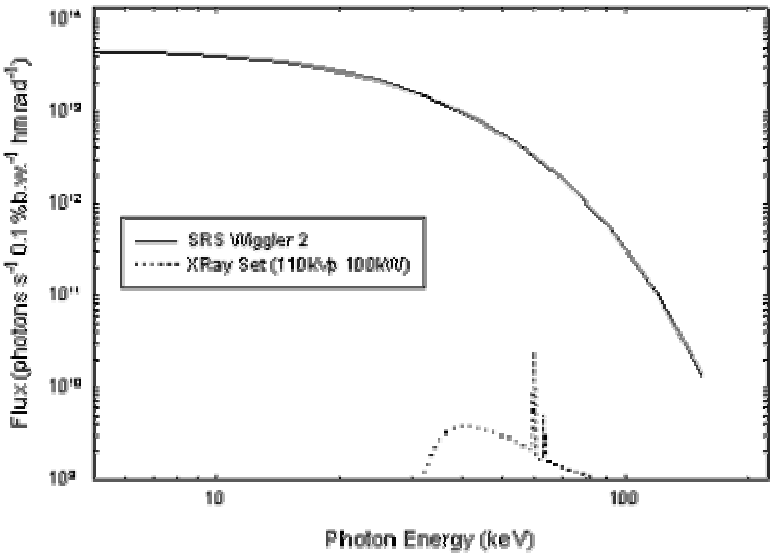

B

Figure 2.2 Comparison of the spectrum of laboratory X-ray radiation from a copper tube (A) with that of synchrotron radiation; the radiation spectrum from the Daresbury Synchrotron Radiation Source[4] (B).

High-temperature synchrotron powder X-ray diffraction measurements were carried out at beamline 11-ID-B of the Advanced Photon Source (APS), Argonne National Laboratory (ANL), Chicago, IL. X-rays were produced using an elliptical multipole wiggler and monochromated using a mosaic silicon crystal in Laue geometry (3.8 degrees θ, Si 511). A MAR 345 image plate detector was used. The X-ray energy and sample to plate distance was determined by measuring patterns from a standard CeO_2 sample at three different sample to detector distances. As the detector was on a well calibrated stage, the differences in the distances between the three measurements were accurately known. The data fitting was done using the software Fit2d.[5] The calibrated energy and wavelength were 90.08929 keV and 0.13762Å, respectively.

The samples were loaded into capillaries and placed in a capillary furnace for the variable temperature measurements (Figure 2.3).

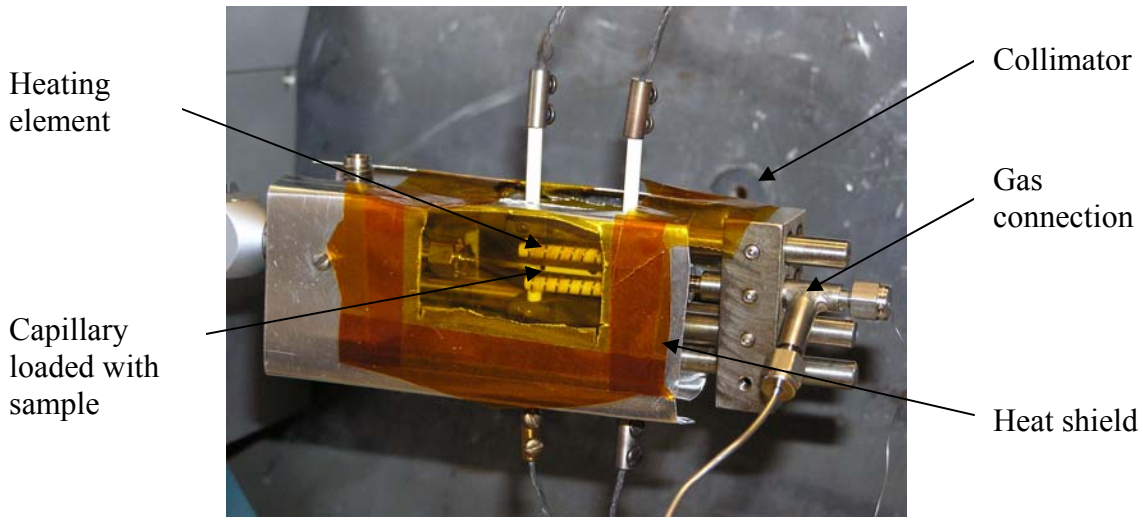

Figure 2.3: Capillary furnace in use at 11-ID-B.

Data collected with the image plate detector were integrated using the Fit2d[5] software. The GSAS[2] program with the EXPGUI[3] graphical user interface was used for the Rietveld refinements of the structural models with the integrated data.

2.3 Thermal Analysis

Thermal analysis methods are powerful techniques for the observation of phase transitions, chemical reactions (e.g. oxidation) and decomposition temperatures using small amounts of solid samples. Crystallizations and structural changes are companied by changes in the heat content of the sample which can be measured by either Differential Scanning Calorimetry (DSC) or Differential Thermal Analysis (DTA). Furthermore, most of the chemical reactions are accompanied not only by changes in the heat content but also in the weight of the sample which can be measured by Thermogravimetric Analysis. Combination of these two techniques, Thermogravimetric/Differential Thermal Analysis (TG/DTA), gives valuable information, in some cases even enough for deducing the chemical reaction.

In a typical TG/DTA experiment, the sample and the reference are in the same furnace and they are heated together. Temperature of the sample and the reference are measured. In addition, the difference in heat required by the sample and reference is calculated. If the thermal event studied, such as melting, requires heat input to the sample (endothermic change), then a negative peak (endotherm) appears in the DTA. Measurement of temperature changes are accompanied by measurement of the weight changes in the sample. If there is evaporation from the sample, it appears as weight decrease; if there is oxidation it appears as weight increase in TG.

The measurements were made with a SEIKO SSC/5200 system TG/DTA 3200 instrument at the School of Polymer, Textile & Fiber Engineering, Georgia Tech. The instrument can be used for experiments up to 1200 °C both in nitrogen and in air. Heating rates and annealing times are programmable.

2.4 X-Ray Fluorescence Spectroscopy

X-Ray fluorescence spectroscopy is a powerful tool for qualitative or quantitative elemental analysis. In this research, it was used to compare the amounts of Ag present in the products of the ion exchange reactions. Samples were measured at room temperature, under air with a Bruker AXS X4 Explorer X-Ray fluorescence spectrometer.

2.5 Scanning Electron Microscopy

Scanning electron microscopy was used to observe differences in the sample before and after oxidation. The scanning electron microscope was a Hitachi X800 Field Emission Gun (FEG) instrument in the Materials Science Engineering Department, Georgia Institute of Technology. Samples were coated with gold before the measurements.

2.6 References

1. JADE *for XRD Pattern Processing*, 6.5.22; Materials Data, Inc.: Livermore, CA, **1995-2005**.

2. Larson, A. C.; Von Dreele, R. B. *General Structural Analysis System*, Los Alamos National Laboratory Report LAUR 86-748; Los Alamos National Laboratory: Los Alamos, NM, **2000**.

3. Toby, B. H., EXPGUI, a graphical user interface for GSAS. *Journal of Applied Crystallography* **2001,** 34, 210-213.

4. http://detserv1.dl.ac.uk/Herald/xray_review_propertiesofsr.htm (Accessed November 01,2005)

5. Hammersley, A. P.; Svensson, S. O.; Hanfland, M.; Fitch, A. N.; Hausermann, D., Two-dimensional detector software: From real detector to idealised image or two-theta scan. *High Pressure Research* **1996,** 14, 235-248.

CHAPTER 3

NEGATIVE THERMAL EXPANSION AND IONIC CONDUCTION IN $GaZr_2(PO_4)_3$

3.1 Introduction

$NaZr_2(PO_4)_3$ is a prototype for a broad family of compounds called "NZP". The structure of $NaZr_2(PO_4)_3$ consists of a three dimensional rigid framework which is stable but flexible. Furthermore, substitution to this framework allows hundreds of different compositions. NZP type compounds show several different properties; ionic conductivity, low and negative thermal expansion, catalytic activity, ferroelectricity, and the ability to immobilize radioactive nuclides. Some NZP structured materials that show negative thermal expansion find commercial applications as coatings[1] and physically and thermally stable, ultra low expansion, insulating ceramics. In addition, materials with high levels of ion exchangeability can find applications in the immobilization of undesired elements from nuclear and fuel reprocessing wastes[2, 3] or as solid state electrolytes[4] or in high energy batteries, etc. NZP-like structures are well known as excellent ionic conductors[5] and recently tetravalent ion conduction was demonstrated in $MNb(PO_4)_3$ (M = Zr, Hf).[6, 7]

There have been a number of publications exploring the chemistry of Ga(I) in halides, coordination compounds and organometallic complexes.[8, 9] However, until the report of Wilkinson[10] on Ga(I)-β''-Alumina and $GaZr_2(PO_4)_3$, there were no well-characterized oxides containing Ga(I). Ga(I)- β –Alumina was first reported by

Radzilowski[11] without detailed crystallographic information. However, its electrical properties and possible applications in the refining of gallium had been investigated.[12,13]

In this chapter, the thermophysical characterization of a $GaZr_2(PO_4)_3$ sample, synthesized by Prof. Wilkinson, is presented.

3.2 Experimental

$GaZr_2(PO_4)_3$ was prepared by ion exchange starting from $AgZr_2(PO_4)_3$ by Dr. Wilkinson.[10] In that synthesis, $AgZr_2(PO_4)_3$ was sealed into an evacuated silica tube with excess amount of gallium and iodine. The tube was annealed for 3 days at approximately 300 ^oC. After the tube was broken open the product was treated with 10% HCl. When the gas evolution was over the product was washed with water. The product was confirmed to be $GaZr_2(PO_4)_3$ by chemical and thermogravimetric analyses in air, powder X-ray diffraction, and XANES.

As part of the current work, high temperature in-situ powder X-ray diffraction data were recorded under low vacuum and nitrogen atmospheres using the equipment in the Materials Science Engineering Department (MSE) at Georgia Institute of Technology. From these results, it was believed that the material was oxidized. Therefore, further experiments were done under reducing atmosphere. Experiments were performed under H_2/N_2 mixture using equipment in the High Temperature Materials Laboratory (HTML) at Oak Ridge National Laboratory. However, from these experiments it was still not certain that the observed was intrinsic to the material. Additional high temperature in-situ diffraction experiments were performed under high vacuum conditions using synchrotron radiation at the Advanced Photon Source (APS), Argonne National Laboratory.

In addition to the above in-situ measurements, several ex-situ experiments were performed under air and in evacuated silica tubes. Thermogravimetric analysis of $GaZr_2(PO_4)_3$ sample under nitrogen is presented. SEM pictures of the original and the oxidized samples are compared.

3.3 Results and Discussion

Dr. Wilkinson's $GaZr_2(PO_4)_3$ sample was used for all the measurements. In order to check if it had degraded, in the 10 years since it was made, a powder X-ray diffraction pattern was recorded. The pattern was fitted using a rhombohedral model, space group R -3 c. The cell parameters and the atomic positions were compared with the published[10] data and it was confirmed that the sample had not changed over time. Refined lattice parameters, the atomic positions and the calculated volume are give in Tables 3.1 and 3.2. No impurity phases could be detected (Figure 3.1).

Table 3.1: Refined Structural Parameters for $GaZr_2(PO_4)_3$

Atom	x	Y	z	10^2U_{11} [a]	10^2U_{22}
Ga(1)	0	0	0	7.3(1)	3.8(2)
Zr(1)	0	0	0.14954(4)	0.43(2)	-
P(1)	0.2872(3)	0	0.25	0.66(6)	-
O(1)	0.1694(4)	-0.0424(4)	0.1985(1)	0.7(1)	-
O(2)	0.1983(4)	0.1720(4)	0.0955(1)	1.0(1)	-

[a] Isotropic temperature factor or U_{11} if an anisotropic temperature factor was refined. *b* $U_{11} = U_{22}$, $U_{12} = 0.5U_{11}$, and $U_{13} = U_{23} = 0$.

Table 3.2: Cell parameters and volume of $GaZr_2(PO_4)_3$

a (Å)	c (Å)	Volume (Å^3)
8.72093(5)	23.8749(2)	1572.52(2)

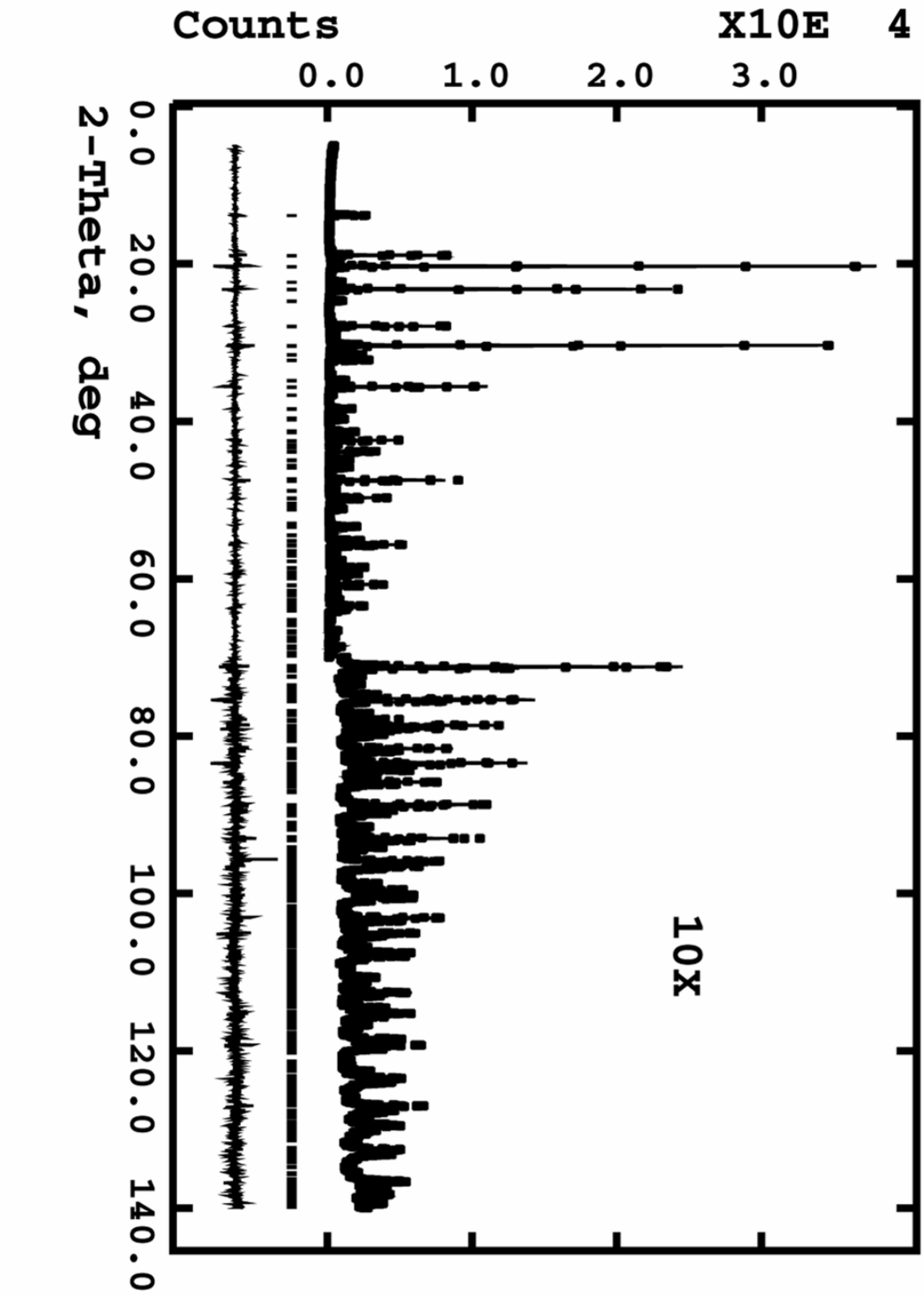

Figure 3.1: Rietveld fit to the powder X-ray diffraction data for $GaZr_2(PO_4)_3$

3.3.1 Thermogravimetric Analysis

TGA experiment on $GaZr_2(PO_4)_3$ in air was previously reported[10]. The material is stable towards oxidation up to ~500 °C. The majority of the weight gain occurred above 650°C, and was complete by 800 °C.

The behavior under nitrogen was determined using equipment in the School of Polymer, Textile & Fiber Engineering, Georgia Tech. A 12.44 mg of sample was put into one platinum pan and an empty pan was used as a reference. The sample was heated at 10 ^oC/min to 1200 ^oC under flowing N_2. There was 0.3% weight loss below 400 ^oC which might be a baseline error in the instrument. Above ~1050 ^oC there was ~3.6% weight loss suggesting evaporation from the sample due to decomposition (Figure 3.2). Detailed information about the decomposition products are given in the Section 3.3.3.

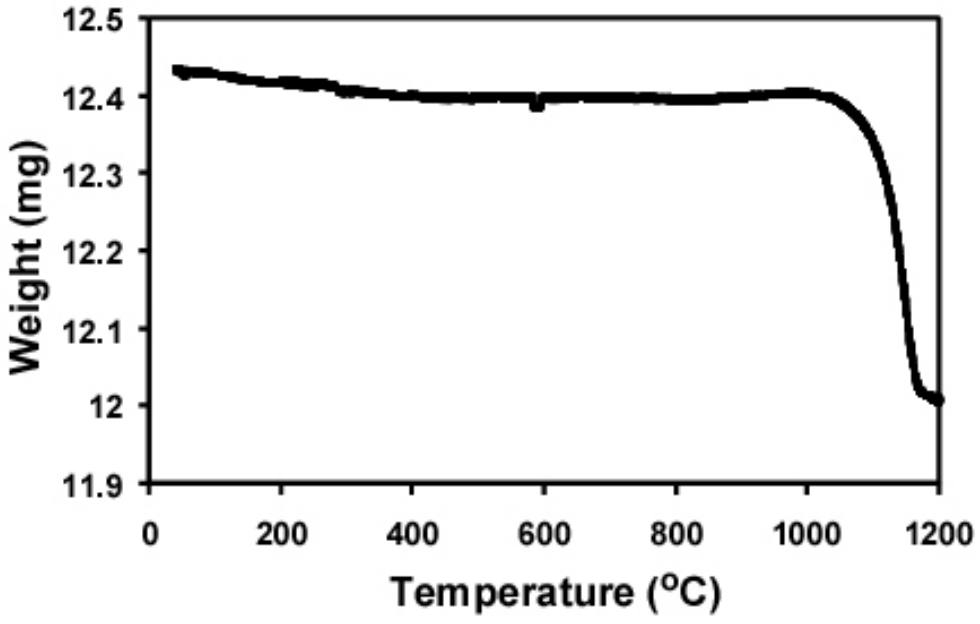

Figure 3.2: Thermogravimetric analysis of $GaZr_2(PO_4)_3$ under nitrogen.

3.3.2 In-Situ High Temperature Diffraction Experiments

3.3.2.1 Experiments Under Low Vacuum and Nitrogen

High temperature in-situ powder X-ray diffraction data were recorded under low vacuum (roughing pump) and nitrogen using an instrument in the X-ray Analysis Group, Materials Science and Engineering (MSE), Georgia Institute of Technology. Both of the experiments were performed using the same temperature program; during heating, data were collected at room temperature and then at 50 ^{o}C intervals up to 900 ^{o}C starting from 50 ^{o}C. In addition, during cooling data were collected every 100 ^{o}C interval down to 100 ^{o}C and then at room temperature. Data were collected on cooling to determine if the thermal expansion behavior of the compound was reversible.

In-situ powder X-ray diffraction data was first recorded under low vacuum. Examination of the X-ray diffraction patterns showed that the sample changes above 600 ^{o}C. However, as the temperature program failed at 900 ^{o}C, data was not collected during cooling and the irreversibility of the change could not be established in this experiment (Figure 3.3).

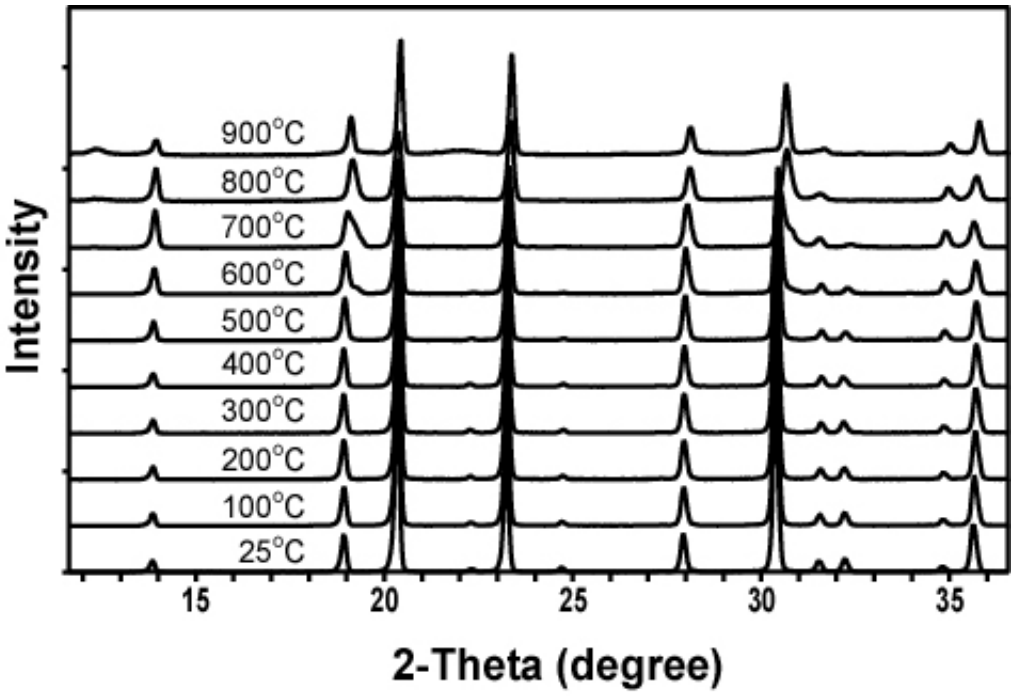

Figure 3.3: Powder X-ray diffraction patterns of $GaZr_2(PO_4)_3$ under vacuum.

The change involving the transformation of one NZP related phase into another NZP type phase. It is believed that the material was oxidized to some extent due to relatively poor vacuum. Further evidence for the oxidization is presented in Section 3.3.3.

Structural analysis was performed up to 700 ^oC using the room temperature model. Above this temperature, there were extra peaks that could not be explained by this model. Plots of a and c as a function of temperature show interesting behavior; below a certain temperature, which is 450 ^oC for a and 350 ^oC for c, a contracts and c expands; however, above these temperatures they do the opposite (Figure 3.6). It is obvious from the volume as a function of temperature plot that the compound is a negative thermal expansion material. However, NTE is only strong above 400 ^oC (Figure 3.7). These changes in the behavior of the cell parameters and the volume at 400 ^oC suggest the onset of a structural or chemical change.

The in-situ experiment was repeated under nitrogen to prevent oxidation. However, it was seen that using nitrogen in this set up does not prevent oxidation (Figure 3.4). The irreversibility of the change was confirmed by collecting data at room temperature during cooling (Figure 3.5). Structural parameters could only be refined up to 700 ^{o}C. Plots of the volume and the cell parameters as a function of temperature show similar behavior to that seen under vacuum. However, the transition temperature is higher. This suggests that the nitrogen provides a less oxidizing atmosphere than the low vacuum in this equipment. Comparison of the cell parameters and the volume from both experiments show that above room temperature there are differences in all the parameters (Figure 3.6 and 3.7).

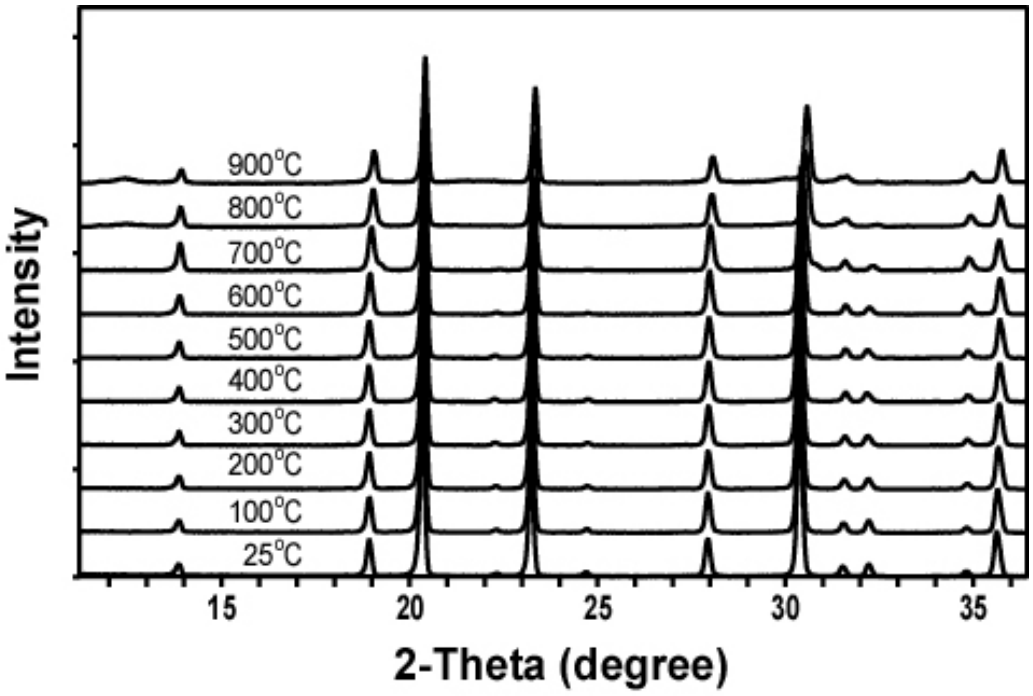

Figure 3.4: Powder X-ray diffraction patterns of $GaZr_2(PO_4)_3$ under nitrogen.

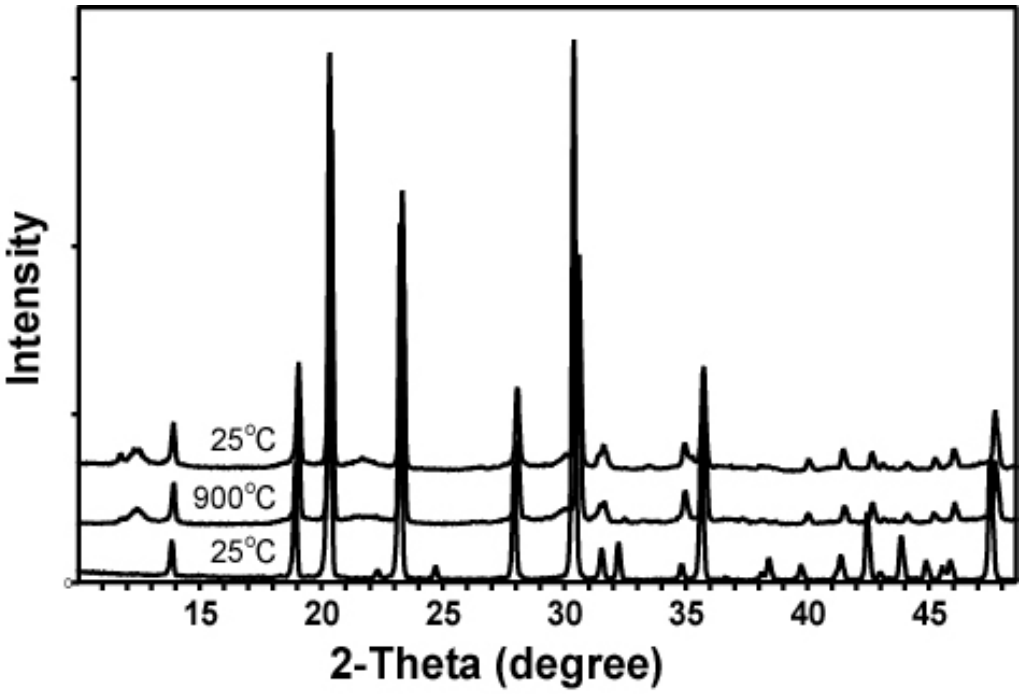

Figure 3.5: Powder X-ray diffraction patterns of $GaZr_2(PO_4)_3$ under nitrogen.

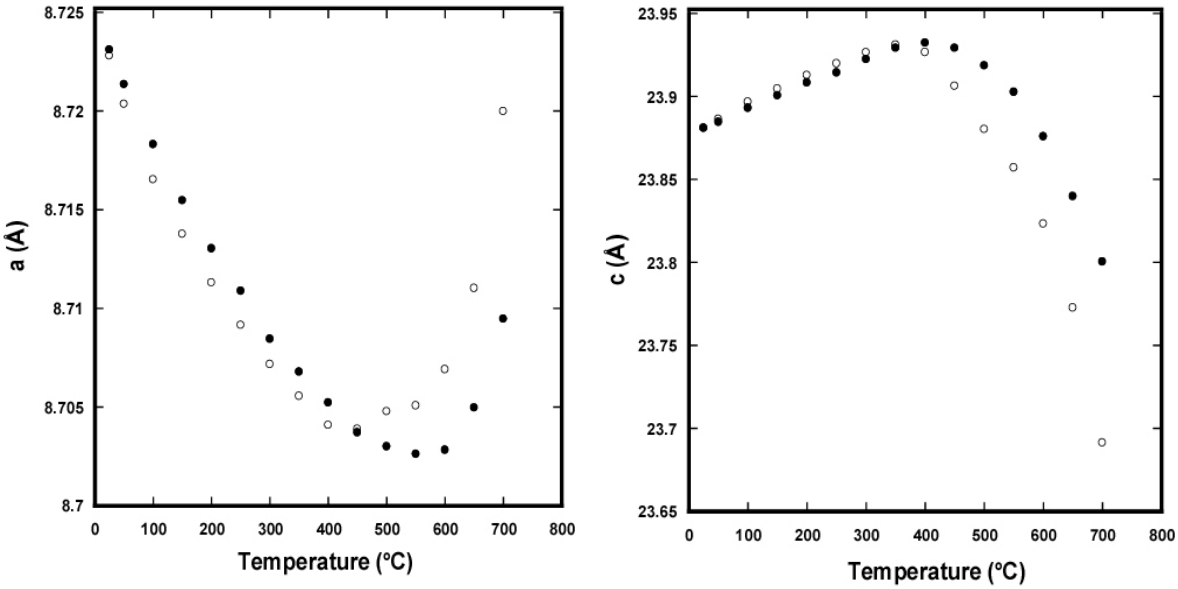

Figure 3.6: Cell parameters, a (Left) and c (Right) for $GaZr_2(PO_4)_3$ as a function of temperature. Solid circles: under nitrogen; Open circles: under vacuum.

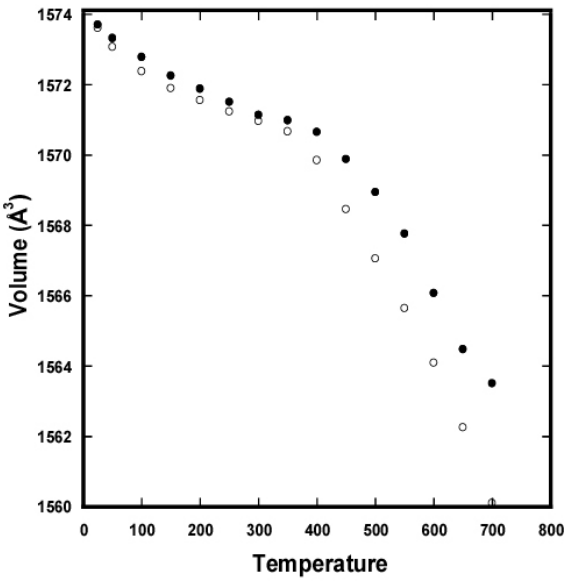

Figure 3.7: Unit cell volume as a function of temperature for $GaZr_2(PO_4)_3$. Solid circles: under nitrogen; Open circles: under vacuum.

3.3.2.2 Experiments Under 4%H_2/96%N_2 Mixture

In order to obtain powder X-ray diffraction data under conditions where oxidation was not an issue, it was decided to perform some experiments using an instrument at the High Temperature Materials Laboratory (HTML), Oak Ridge National Laboratory a reducing atmosphere, 4%H_2/96%N_2 mixture.

It was believed based on the experiments using the MSE equipment that the sample did not change below 400 ^oC. Therefore, data was collected at room temperature and then at 50 ^oC intervals from 50 ^oC up to 900 ^oC. For temperatures above 300 ^oC, the sample was cooled back to 300 ^oC and a data set collected prior to further increasing the temperature to see if the observed changes were reversible. After reaching 900 ^oC, data were collected at 200 ^oC intervals on cooling to 300 ^oC and then the sample was cooled to room temperature. The powder diffraction patterns did not show any major changes up to

900 ^{o}C, unlike the earlier experiments in low vacuum and nitrogen. A structural model could be refined using all the data collected at all temperatures up to 900 ^{o}C (Figure 3.8).

Changes in the cell parameters and unit cell volume with temperature are shown in Figures 3.9 and 3.10. The cell parameters and volume at 300 ^{o}C depend upon the samples thermal expansion. If the sample is cooled to 300 ^{o}C from a higher temperature, the cell parameter a increases. However, the c parameter determined at 300 ^{o}C gets smaller up to 800 ^{o}C and than gets bigger. The volume decreases at 300 ^{o}C if it is cooled from a temperature below 650 ^{o}C and expands if it is cooled from a higher temperature (Figures 3.11 and 3.12).

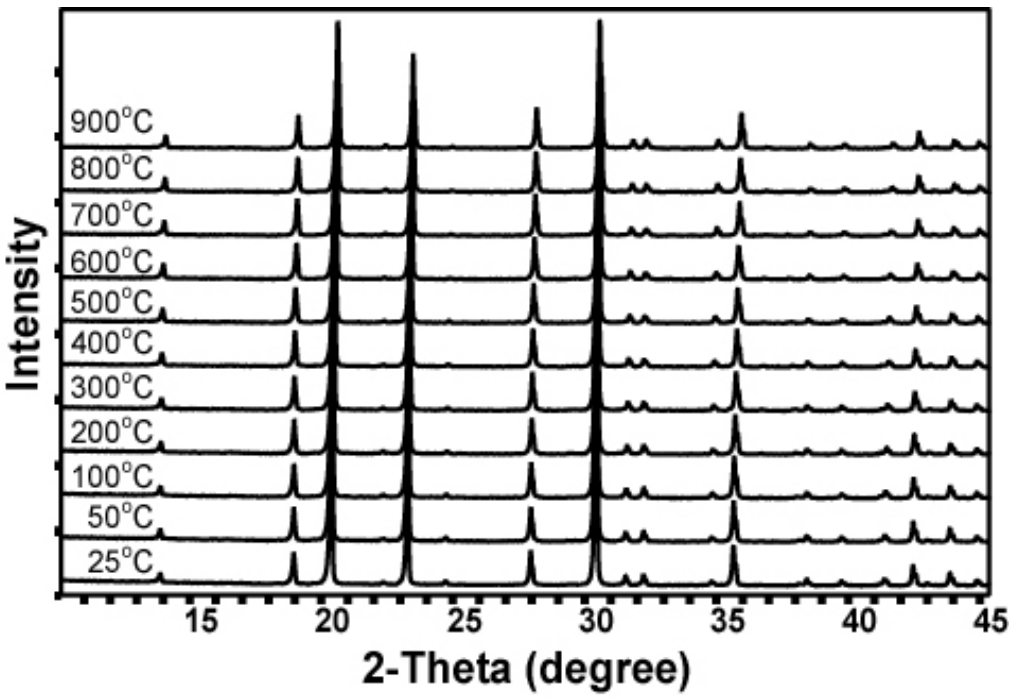

Figure 3.8: Powder X-ray diffraction patterns of $GaZr_2(PO_4)_3$ under H_2/N_2 mixture. There are no profile changes in the patterns.

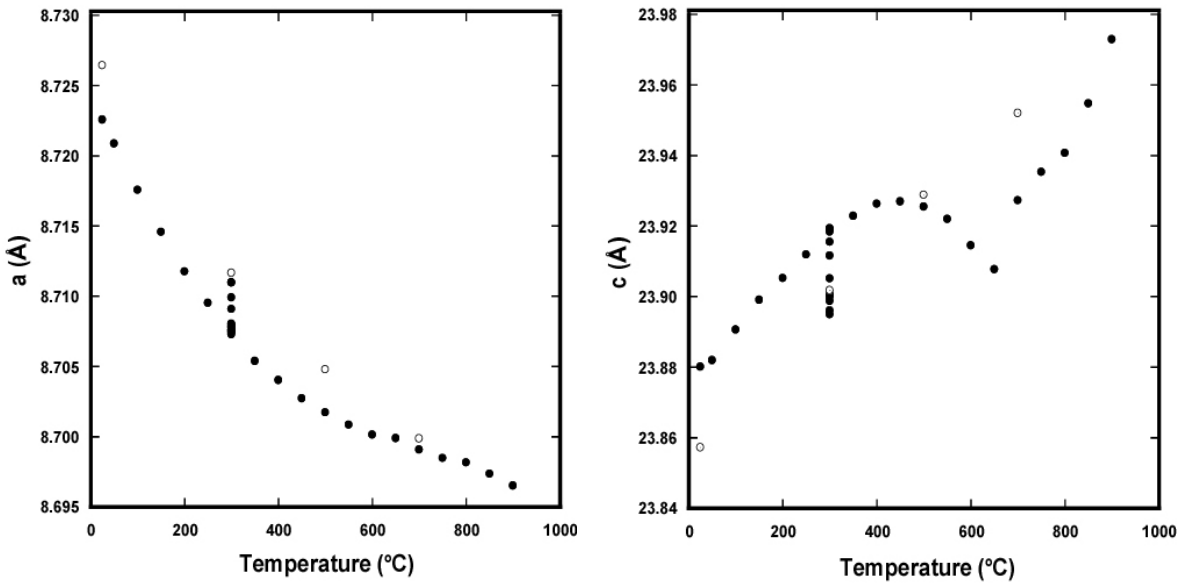

Figure 3.9: Cell parameters, a (Left) and c (Right) of $GaZr_2(PO_4)_3$ as a function of temperature. Experiment in H_2/N_2 mixture. Solid Circles: on heating; Open Circles: on cooling.

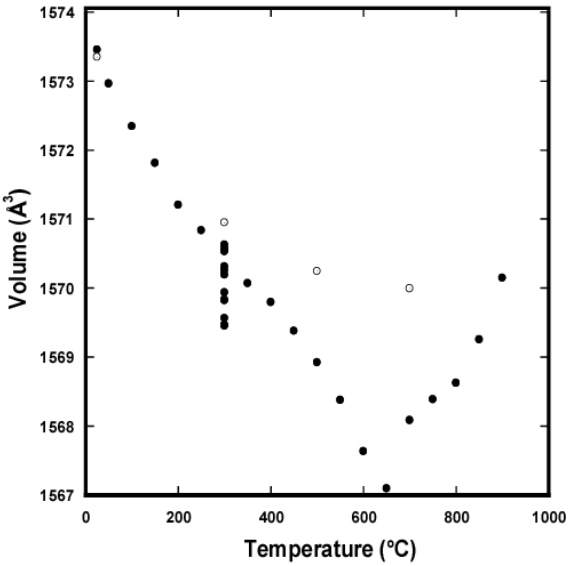

Figure 3.10: Unit cell volume for $GaZr_2(PO_4)_3$ as a function of temperature. Experiment in H_2/N_2 mixture. Solid Circles: on heating; Open Circles: on cooling.

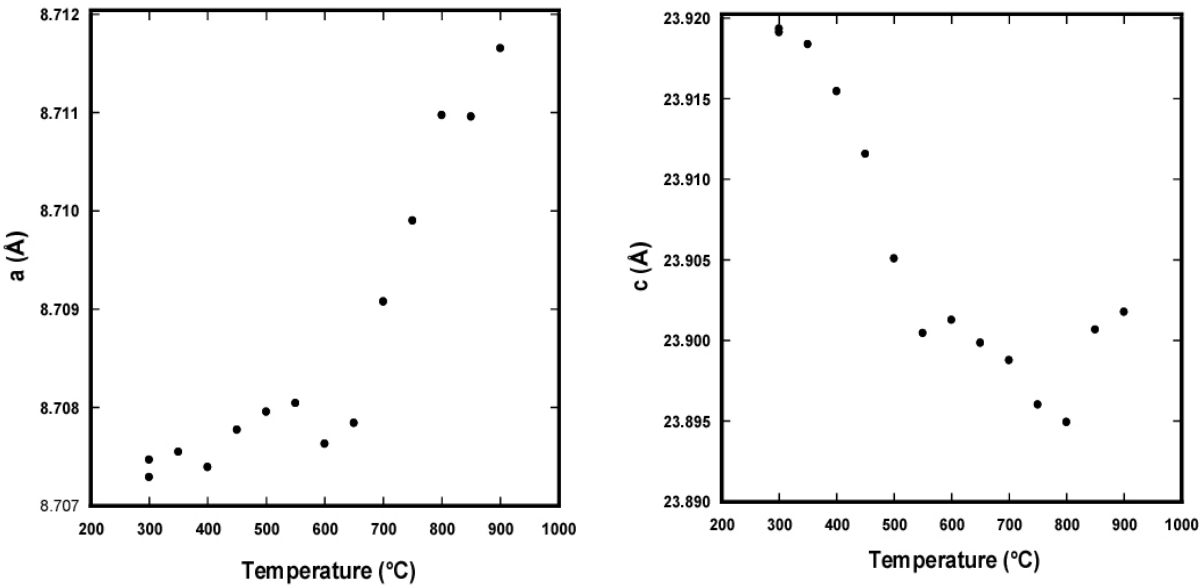

Figure 3.11: Cell parameters, a (Left) and c (Right) for $GaZr_2(PO_4)_3$ at 300 ^oC as a function of the temperature at which it was prior to cooling back to 300 ^oC. Experiment in H_2/N_2 mixture.

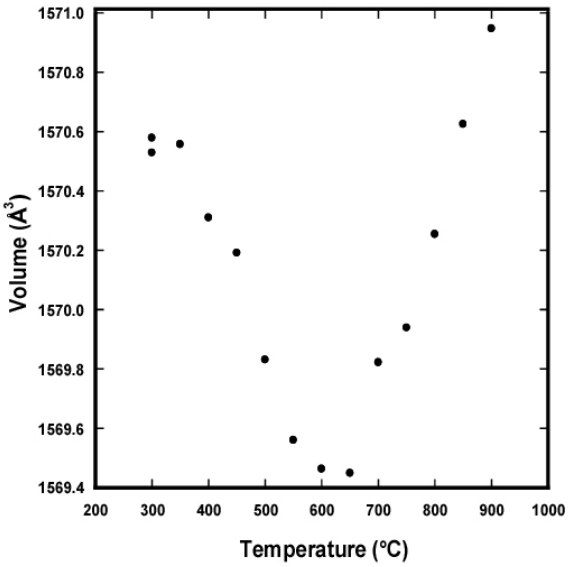

Figure 3.12: Unit cell volume for $GaZr_2(PO_4)_3$ at 300 ^oC as a function of temperature at which it was prior to cooling back to 300 ^oC. Experiment in H_2/N_2 mixture.

From these results it seemed possible that Ga(I) was not at its most thermodynamically stable position in the original sample and that the repeated heat treatments lead to a redistribution of it associated with changes in the lattice constants. Therefore, it was decided to collect data at temperatures above 400^{o}C repeatedly and see if the material reached an equilibrium state. This experiment was done under the same atmosphere, H_2/N_2 mixture, as the other experiment, and each powder pattern was recorded in 15 minutes. The temperature was initially increased to 500 ^{o}C and then data were collected. After recording 6 powder X-ray diffraction patterns it was decided that the sample was no longer changing. The instrument was then programmed to record 44 powder patterns at 700 ^{o}C and then a further 28 patterns at 500 ^{o}C. Finally, data were collected at room temperature.

The refined cell parameters as a function of time/temperature show that at 700 ^{o}C the a parameter increases and the c parameter decreases with time. After 11 hours the cell parameter did not stabilize; c started to increase. When the temperature was reduced back to 500 ^{o}C, there were no significant changes in the lattice constants with time. However, the cell parameters and volume are significantly different than the ones previously obtained at 500 ^{o}C indicating that the changes at 700 ^{o}C are irreversible on a time scale of many hours.(Figures 3.13 and 3.14).

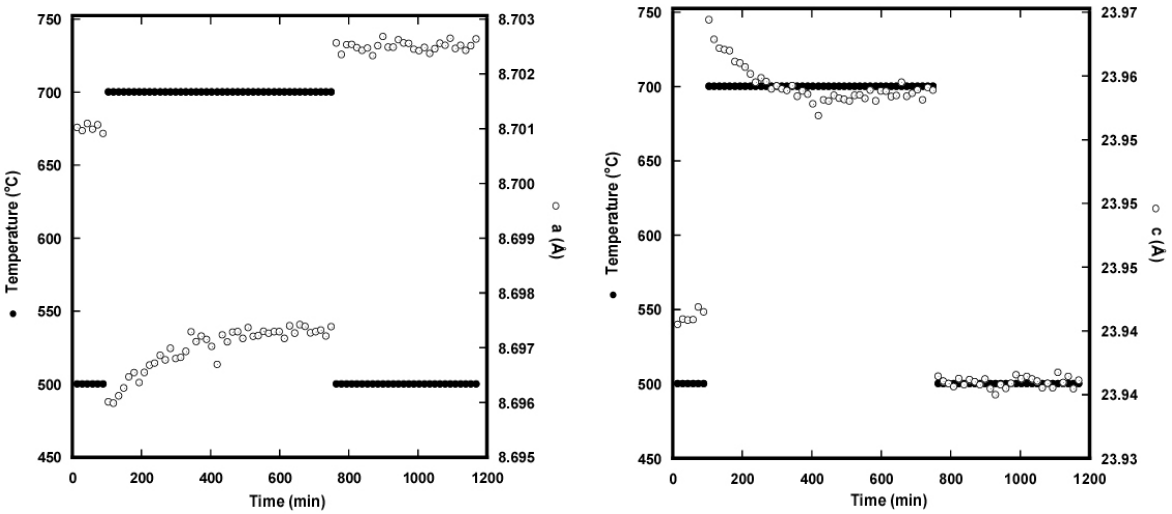

Figure 3.13: Cell parameters, a (left) and c (right), and temperature as a function of time. Experiment in H_2/N_2 mixture. Solid circles: temperature; open circles: the unit cell parameters.

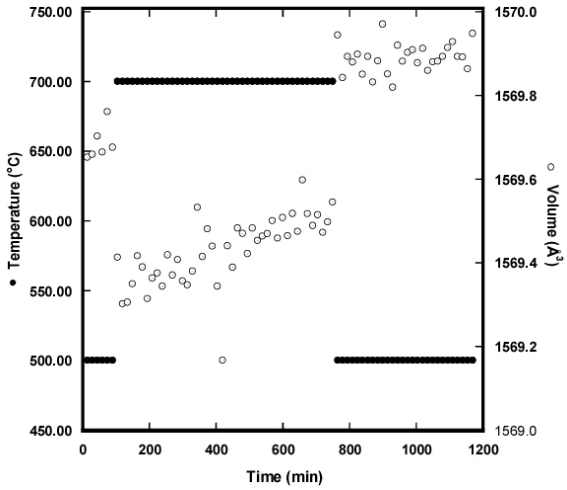

Figure 3.14: Unit cell volume for $GaZr_2(PO_4)_3$ and the temperature as a function of time. Experiment in H_2/N_2 mixture. Solid circles: temperature; open circles: unit cell volume.

In order to further investigate the material's thermal expansion characteristics, it was decided to collect data repeatedly at 600 ^oC, 800 ^oC and 900 ^oC. These experiments showed that the cell parameters and the volume of the material do not change at 600 ^oC,

except the initial heating, with time but the cell parameters at 600 ^{o}C depend on the sample's thermal history. In addition, if the material is cooled to 600 ^{o}C from a higher temperature than the previous cell parameter a increases and c decreases (Figures 3.15 and 3.16).

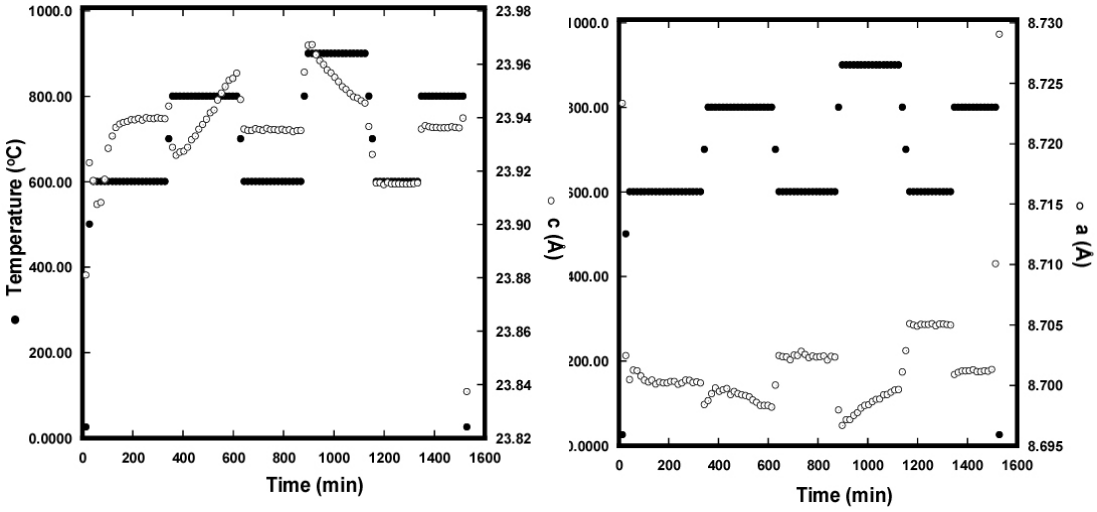

Figure 3.15: Cell parameters, a (left) and c (right), and temperature as a function of time. Experiment in H_2/N_2 mixture. Solid circles: temperature; Open circles: the unit cell parameters.

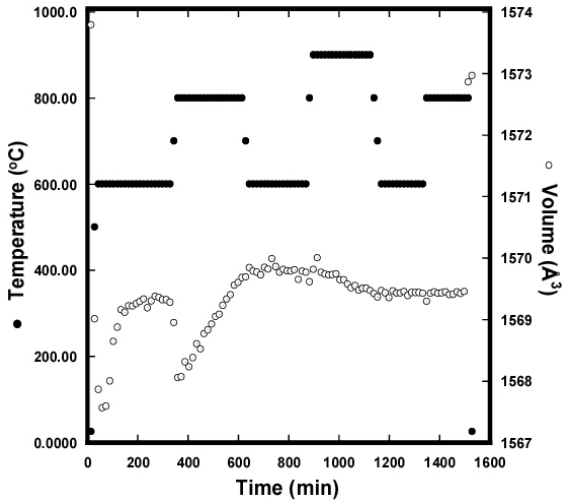

Figure 3.16: Unit cell volume of $GaZr_2(PO_4)_3$ and the temperature as a function of time. Experiment in H_2/N_2 mixture. Solid circles: temperature; Open circles: unit cell volume.

3.3.2.3 Experiment Under High Vacuum Using Synchrotron Radiation

Further experiments were performed using synchrotron radiation at the Advanced Photon Source (APS), Argonne National Laboratory (ANL), Chicago. $GaZr_2(PO_4)_3$ was put into a 1 mm quartz capillary and held in place with some silica wool. One end of the capillary was cut off and the other end kept closed. The capillary was mounted in a home made furnace as shown in Section 2.2. The system was connected to a turbo pump and the pressure was noted after each measurement. Before the experiment, the temperature of the sample went up to 300 ^oC because of a problem in the temperature controller and the furnace was turned off. The experiment was started when the sample cooled back to room temperature. Data were recorded at room temperature and then at 50 ^oC intervals starting from 50 ^oC up to 800 ^oC. On cooling, data were collected every 100 ^oC down to 200 ^oC, except 700^oC, and then at room temperature. The acquisition of each diffraction pattern took 4 minutes and then the temperature controller was manually set to the next

temperature. The pressure was between $5.6x10^{-6}$ and $4.8x10^{-6}$ Torr until 200 ^{o}C on cooling. At 200 ^{o}C, on cooling the pressure was $1.9x10^{-2}$ Torr. After the experiment, it was seen that the capillary was broken.

The hysteresis that was observed in the previous experiments was also seen in this experiment; the cell parameters and the volume are different on heating and cooling for a given temperature (Figure 3.17 and 3.18). As the pressure was around 10^{-6} Torr throughout the experiment it is unlikely that there is any oxidation. The hysteresis is either due to a structural change or evaporative loss from the sample. The very different behavior at ~400 ^{o}C and above in high vacuum from that observed in low vacuum and nitrogen on the instrument in MSE suggests that the sample in low vacuum and nitrogen was under going oxidation even at 400 ^{o}C.

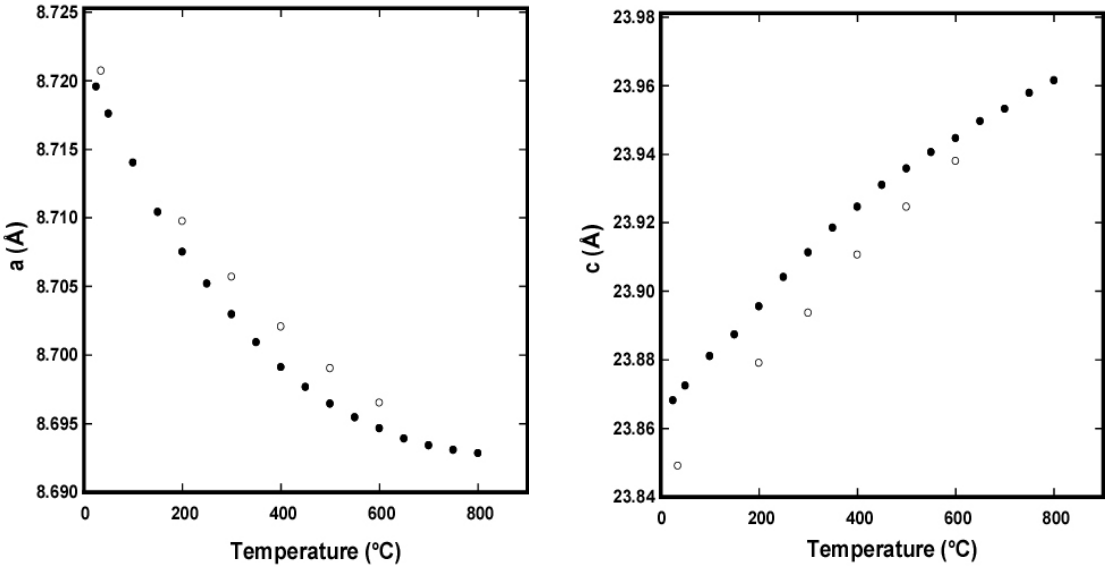

Figure 3.17: The cell parameters, a (left) and c (right), as a function of temperature for $GaZr_2(PO_4)_3$. Synchrotron experiment under high vacuum. Solid Circles: on heating; Open Circles: on cooling

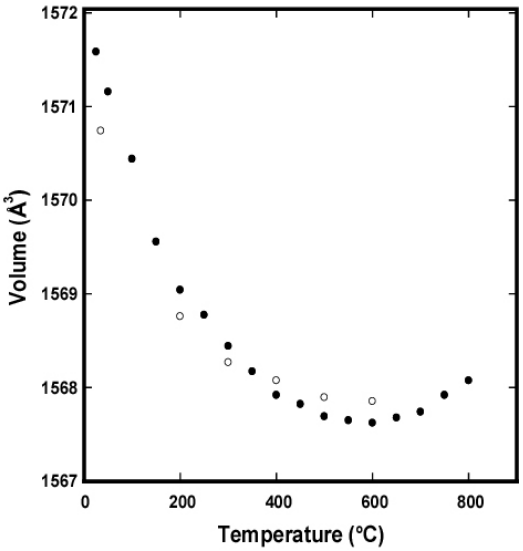

Figure 3.18: Unit cell volume of $GaZr_2(PO_4)_3$ as a function of temperature. Synchrotron experiment under high vacuum. Solid Circles: on heating; Open Circles: on cooling.

3.3.3 Ex-Situ Diffraction Experiments

3.3.3.1 Experiments Under Air

Approximately 0.5 grams of $GaZr_2(PO_4)_3$ were put into an open quartz tube. The tube was initially heated to 650 ^oC for 12 hours and then oven cooled to room temperature. The weight gain of %3.01 is in a good agreement with the expected weight gain of %2.99 from the oxidation of Ga(I) to Ga(III). The powder pattern of the product had very similar peak positions to that of the known NZP type phase $SrZr_4(PO_4)_6$ (Figure 3.19). From these measurements it is believed that the composition of the material is "$Ga_{1/3}Zr_2(PO_4)_3$". However, no Ga_2O_3 could be detected. Several structural models for the phase were explored, but no satisfactory fit to the powder pattern could be obtained.

The synthesis of $GaZr_2(PO_4)_3$ by ion exchange at 300 ^oC indicates that Ga(I) is mobile at this temperature. As the oxidized product has an NZP structure, we believe that Ga(I) migrates to the surface and reacts with oxygen. It was decided to get some SEM

data on the original and the oxidized samples and look for any sign of oxidation product on the NZP phase's surface. However, the SEM pictures showed no change after oxidation. (Figure 3.22)

The ex-situ oxidized sample was reheated to 700 ^{o}C, 750 ^{o}C, 850 ^{o}C, 950 ^{o}C, 1000 ^{o}C, and 1050 ^{o}C for 12 hours at each temperature and after each heat treatment it was oven cooled to room temperature. Powder patterns and the weights of the samples were recorded (Figure 3.21). Between 700 ^{o}C and 1000 ^{o}C, on the low angle side of the powder pattern a peak, which could not be identified, formed and then disappeared at 1050 ^{o}C. The sample started to loose weight around 1000 ^{o}C and decomposed to $Ga(PO_4)_3$, ZrO_2, Zirconia and ZrP_2O_7 at 1050 ^{o}C (Figure 3.22).

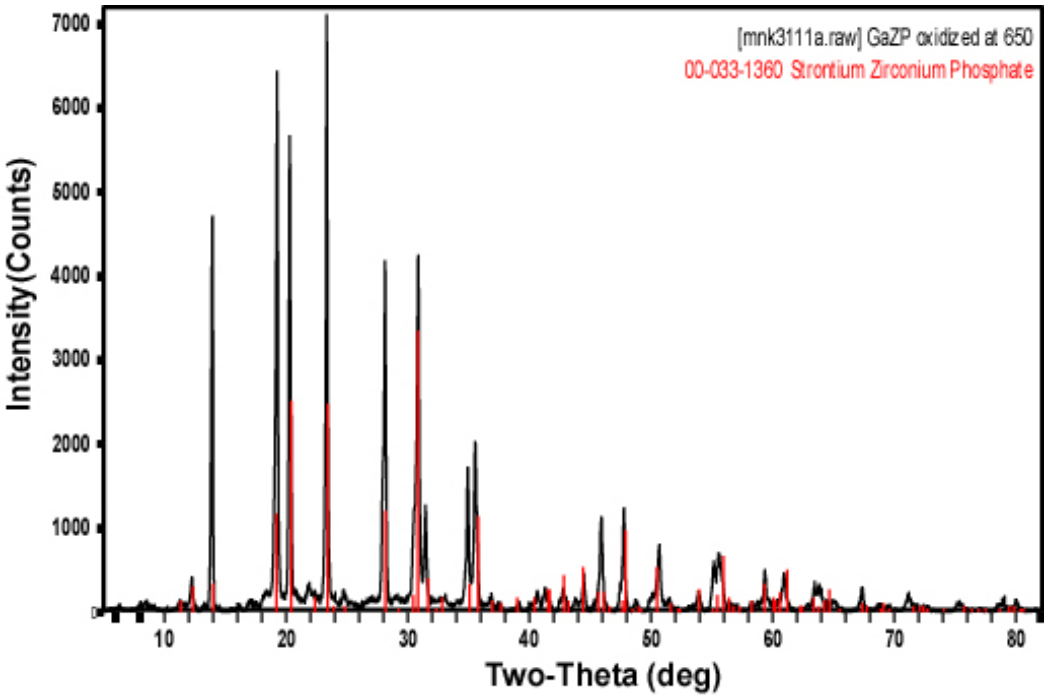

Figure 3.19: Powder diffraction pattern of the oxidized $GaZr_2(PO_4)_3$ at 650 ^{o}C under air. Peak positions match the NZP type phase $SrZr_4(PO_4)_6$.

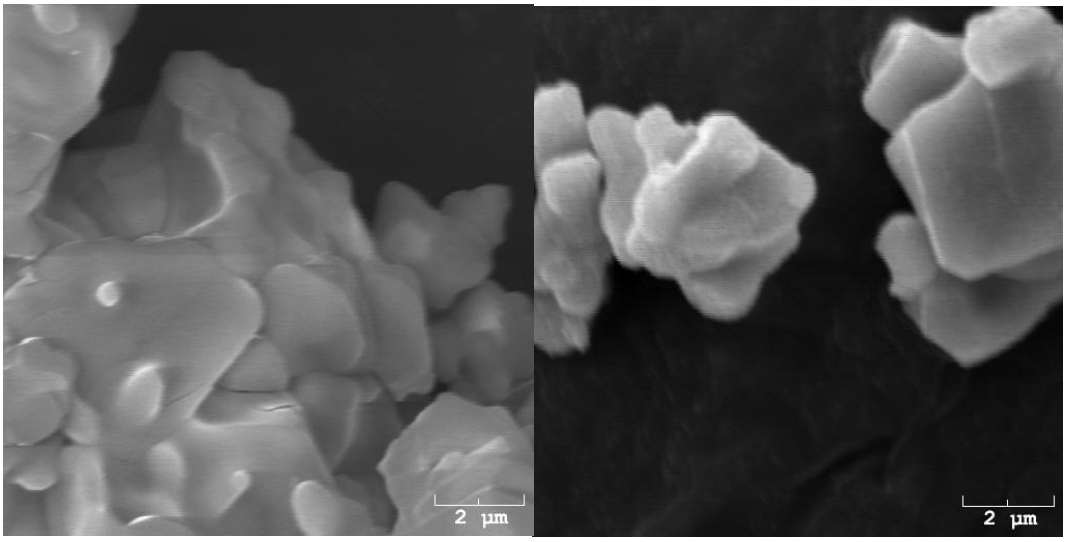

Figure 3.20: SEM pictures of (left) the original $GaZr_2(PO_4)_3$ and (Right) the oxidized $GaZr_2(PO_4)_3$

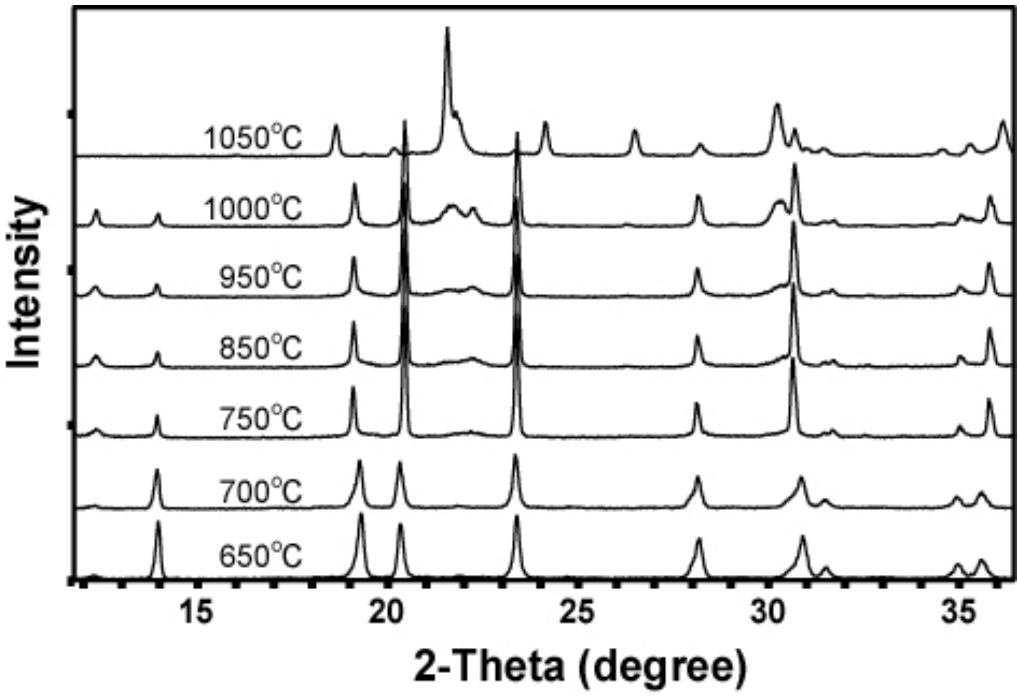

Figure 3.21: Powder diffraction patterns of $GaZr_2(PO_4)$ after heating in air at the indicated temperature.

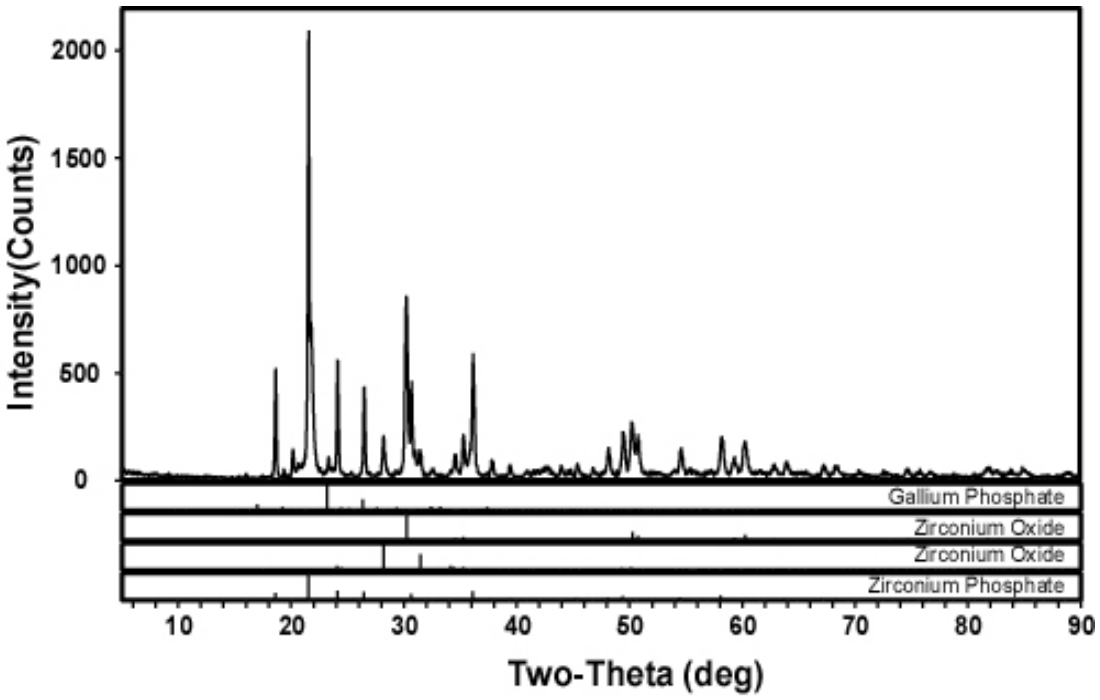

Figure 3.22: Powder X-ray diffraction data for $GaZr_2(PO_4)_3$ after annealing at 1050 ^oC.

Direct synthesis of "$Ga_{0.33}Zr_2(PO_4)_3$" was attempted by mixing Ga_2O_3, ZrO_2 and $(NH_4)H_2(PO_4)_3$. Mixed reactants were initially heated to 600 ^oC for 6 hours and then heated to 900 ^oC for 36 hours after which sample was oven cooled to room temperature and powder X-ray diffraction pattern was recorded. The sample was ground and reheated to 1100 ^oC for 36 hours and powder X-ray diffraction pattern was recorded. The powder patterns were indexed to ZrP_2O_7, $Ga(PO_4)$, and ZrO_2. No other phase could be detected.

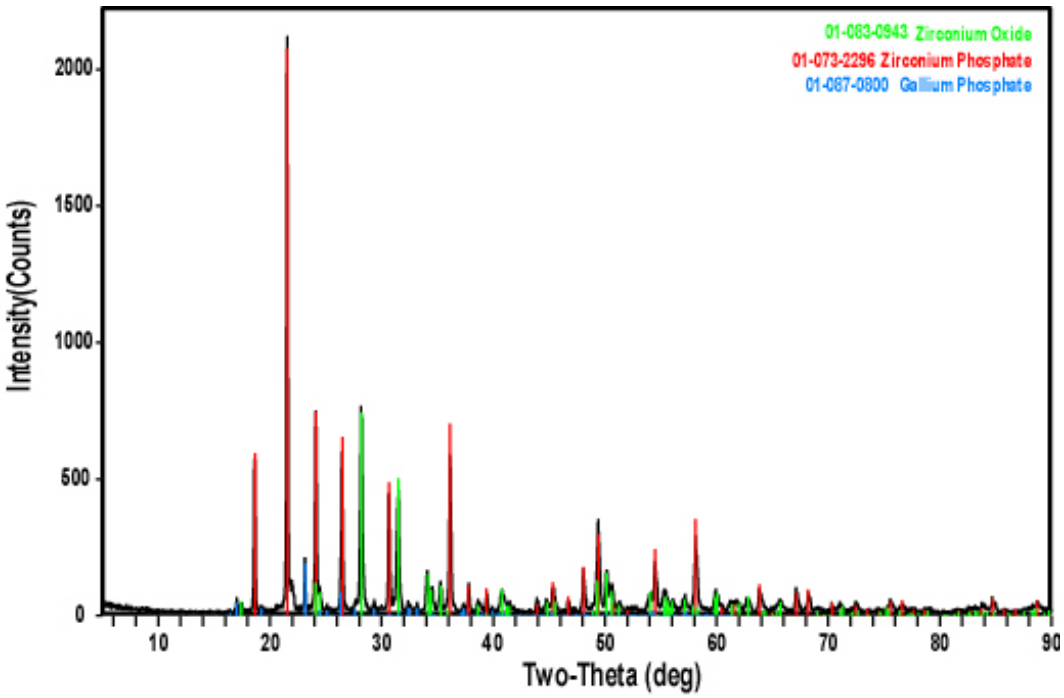

Figure 3.23: Powder pattern of the product after the direct reaction of Ga_2O_3, ZrO_2 and $NH_4H_2(PO_4)_3$ at 1100 ^oC.

3.3.3.2 Experiments in Evacuated Fused Silica Ampoules

In order to understand if the changes in the lattice parameters observed in the in-situ experiments are due to oxidation, 0.5 grams of $GaZr_2(PO_4)_3$ were sealed into evacuated silica tubes and heated to 950 ^oC for 12 hours. One of the tubes was oven cooled and the other one was quenched by dropping the tube into water. The tubes were broken open and powder X-ray diffraction patterns of the samples were recorded. There were no obvious changes in the powder patterns on carrying out the heat treatments. Rietveld refinements of the samples' structures were performed. Comparison of the cell parameters and volumes showed that the samples are significantly different than each other as well as from the original sample (Table 3.3). As the samples were sealed into evacuated tubes these changes are not due to oxidation. The differences between the

original sample and the samples heated to in sealed evacuated silica tubes could be attributed to a structural change or evaporative loss. If it is irreversible structural change or evaporative loss, then quenching might have stopped the change earlier than the oven cooled sample causing differences between the samples.

Table 3.3: Cell parameters and volume of heat treated $GaZr_2(PO_4)_3$ compared to the original sample.

Material	Temperature (^oC)	Treatment	a (Å)	c (Å)	Volume ($Å^3$)
$GaZr_2(PO_4)_3$	Room Temp.	Original	8.72093(5)	23.8749(2)	1572.52(2)
$GaZr_2(PO_4)_3$	Room Temp.	Oven cooled from 950^oC	8.72238(5)	23.8760(2)	1573.12(2)
$GaZr_2(PO_4)_3$	Room Temp.	Quenched from 950^oC	8.72351(5)	23.8664(2)	1572.89(2)

It is well known that NZP structured materials may show excellent ionic conductivity. Recently, it was reported[6, 7] that even tetravalent ionic conduction is possible. Therefore, it was decided to measure the ionic conductivity of the material. A pellet was pressed and sealed into an evacuated silica tube and put into the furnace. The sintering temperature was set as 950 ^{o}C. However, the temperature went up to 1200 ^{o}C, which is higher than the decomposition temperature, because of a programming error. When the tube was broken open, it was seen that brown needle-like crystals had grown on the surface of the pallet. EDX measurements, using the SEM instrument in the Materials Science Engineering at Georgia Institute of Technology which can detect elements with Z > 8, showed that the elements present in the crystals are Ga, P and Fe. Source of the iron could be the die that used to press the pellet. In addition, crystals were sent to Emory University for single crystal X-ray diffraction measurements. The unit cell

of the material was determined tentatively to be hexagonal with a = 3.85 Å and c = 9.42 Å. However, the structure has not yet been solved.

Another pellet was prepared and sealed in an evacuated silica ampoule. It was heated to 950 ^{o}C for 12 hours, after which it was broken open. It was seen that there was brown residue at the surface of one end of the tube. This residue was not observed during the previous experiments under same conditions. In the previous experiments the amount of the sample was a quarter of the amount used to prepare the pellet. In addition, it is believed that because of very low amount, the residue could not be detected. Powder X-ray diffraction of the residue was recorded and it was seen that it contains crystalline $Ga(PO_4)$. It is known that $Ga(PO_4)$ is white and nonvolatile. Therefore, the brown compound could be amorphous. As the color of the residue was similar to that of the single crystals formed at 1200 ^{o}C, it seems possible that it is the same compound.

3.4 Conclusion and Outlook

Comparison of the data collected using the equipment in the Materials Science Engineering Department (MSE) at Georgia Institute of Technology, High Temperature Materials Laboratory (HTML) at Oak Ridge National Laboratory and at the Advanced Photon Source (APS) at Argonne National Laboratory confirms that the behavior observed at MSE is the oxidation of the sample due to poor inert conditions. The differences below 300 ^{o}C between the APS and HTML data may be attributed to the initial uncontrolled temperature increase to 300 ^{o}C at APS, and the variations because of the temperature programs, the data collection times and the uncertainty in the wavelength of the APS data. In addition, the differences above 300 ^{o}C could be the result of the different temperature programs (Figure 3.24 and 3.25).

The long time scale changes observed during in-situ powder X-ray diffraction measurements under H_2/N_2 mixture suggests a chemical reaction with H_2 and/or N_2, or a diffusion limited structural change, or evaporative loss from the sample.

The differences between the original sample and the samples heated to 950 ^oC in sealed evacuated silica tubes could also be attributed to a structural change or evaporative loss. If it is irreversible structural change or evaporative loss, then quenching might have stopped the change earlier than the oven cooled sample causing differences between the samples.

The structure of the brown crystals that were formed at 1200 ^oC inside the evacuated quartz tube needs to be solved. If there is evaporation from the sample at high temperatures, this may change the lattice constants of the material and the identification of the crystals may give insight into this issue. TG data can be collected for a very long time at a constant temperature to see if there are any changes under inert atmosphere to determine if the time dependence seen in Figure 3.13 and 3.15 are due to evaporation.

Ionic conductivity of the original material and "$Ga_{0.33}Zr_2(PO_4)_3$" should be measured.

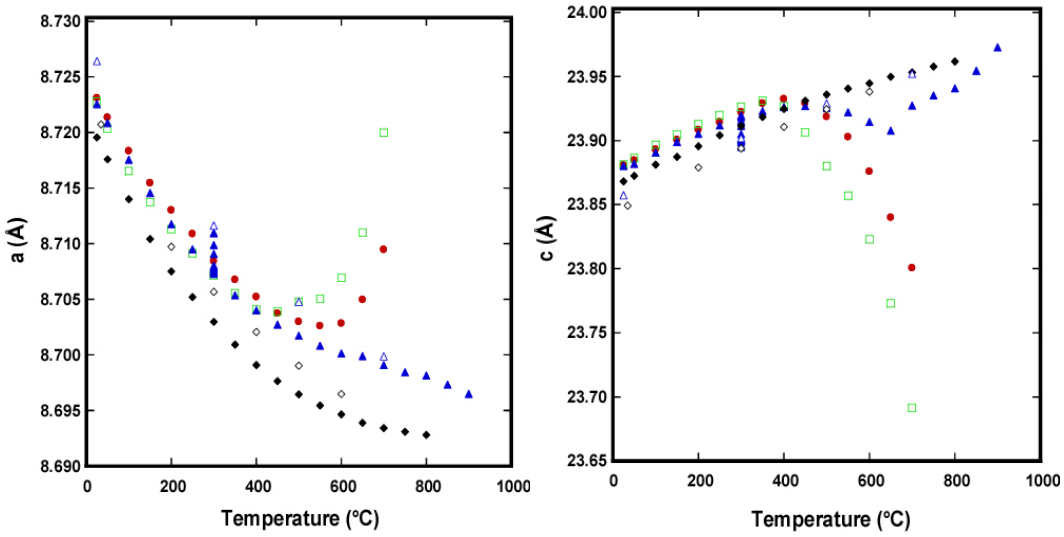

Figure 3.24: Cell parameters, a (left) and c (right), as a function of temperature for $GaZr_2(PO_4)_3$. Data collected at APS; Solid Circles: on heating; Open Circles: on cooling. Data collected at ORNL; Solid blue triangles: on heating; Open blue triangles: on cooling. Data collected at MSE; Open green squares: under vacuum ; Solid red circles: under nitrogen.

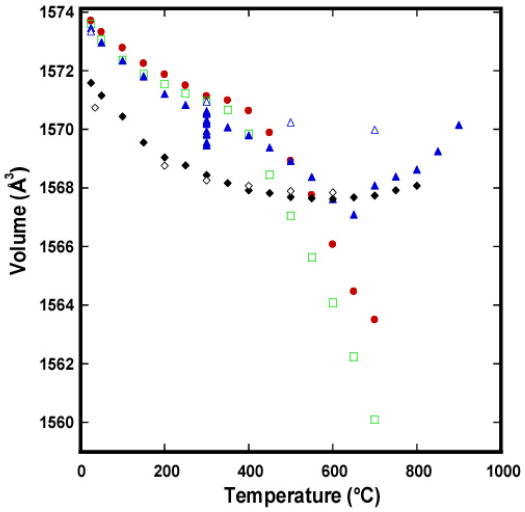

Figure 3.25: Unit cell volume as a function of temperature for $GaZr_2(PO_4)_3$. Data collected at APS; Solid Circles: on heating; Open Circles: on cooling. Data collected at ORNL; Solid blue triangles: on heating; Open blue triangles: on cooling. Data collected at MSE; Open green squares: under vacuum; Solid red circles: under nitrogen.

3.5 References

1. Lee, W. Y.; Cooley, K. M.; Berndt, C. C.; Joslin, D. L.; Stinton, D. P., High-temperature chemical stability of plasma-sprayed Ca0.5Sr0.5Zr4P6O24 coatings on Nicalon/SiC ceramic matrix composite and Ni-based superalloy substrates. *Journal of the American Ceramic Society* **1996,** 79, (10), 2759-2762.

2. Pet'kov, V. I.; Orlova, A. I.; Trubach, I. G.; Asabina, Y. A.; Demarin, V. T.; Kurazhkovskaya, V. S., Immobilisation of nuclear waste materials containing different alkali elements into single-phase NZP-based ceramics. *Czechoslovak Journal of Physics* **2003,** 53, A639-a648.

3. Pet'kov, V. I.; Sukhanov, M. V., Immobilisation of molybdenum from fuel reprocessing wastes into sodium zirconium phosphate ceramics. *Czechoslovak Journal of Physics* **2003,** 53, A671-a677.

4. Imanaka, N.; Adachi, G.-y., Rare earth contribution in solid state electrolytes, especially in the chemical sensor field. *Journal of Alloys and Compounds* **1997,** 250, 492-500.

5. Alamo, J., Chemistry and properties of solids with the [NZP] skeleton. *Solid State Ionics* **1993,** 63-65, 547-561.

6. Imanaka, N.; Itaya, M.; Ueda, T.; Adachi, G., Tetravalent Zr4+ or Hf4+ ion conduction in NASICON type solids. *Solid State Ionics* **2002,** 154, 319-323.

7. Imanaka, N.; Ueda, T.; Okazaki, Y.; Tamura, S.; Hiraiwa, M.; Adachi, G. Y., Tetravalent ion(Zr4+) conduction in solids. *Chemistry Letters* **2000**, (5), 452-453.

8. Greenwood, N. N., The Chemistry of Gallium. *Advances in Inorganic Chemistry and Radiochemistry* **1963,** 5, 91-134.

9. Greenwood, N. N.; Earnshaw, A., *Chemistry of the Elements*; Pergamon Press: **1984**.

10. Wilkinson, A. P., Crystal Chemistry of Ga(I) in Oxides: Ga^{+}-β"-Alumina and $GaZr_2(PO_4)_3$. *Inorganic Chemistry* **1997,** 36, 1602-1607.

11. Radzilow.Rh, Preparation of Gallium (I) Beta-Alumina. *Inorganic Chemistry* **1969,** 8, 994-996

12. Pitt, M. G.; Fray, D. J., Electrical Properties of Indium and Gallium Beta Alumina. *Electrochimica Acta* **1982,** 27, 15-24.

13. Gee, R.; Fray, D. J., Refining of Gallium using Gallium Beta-Alumina. *Electrochimica Acta* **1979,** 24, 765-767.

CHAPTER 4

SYNTHESIS AND CHARACTERIZATION OF $InZr_2(PO_4)_3$

4.1 Introduction

Indium(I) chemistry has been studied in halides, organometallic complexes, and coordination compounds.[1-3] However, there are only a small number of well characterized In(I) oxides due to the instability of In(I). Some structural information is available for matrix isolated and gas phase In_2O.[4, 5] In addition, there are reports on the catalytic activity of In(I) incorporated in zeolites for the reduction of nitric oxides with hydrocarbons in the presence of oxygen.[6, 7] However, except for reports on In_xWO_3[8], In(I) β-Alumina[9, 10] and $In_2P_2O_7$[11] there are no well-characterized In(I) oxides in the solid state. Luckily, Pitt's strategy for the synthesis of In(I) β-Alumina by ion exchange can be adapted for any material that has ionic conductivity at moderate temperatures.

Ionic conductivity of materials with the Sodium Zirconium Phosphate (NZP) like frameworks has been investigated extensively. In addition, because of their potential applications as ionic conductors, and very low or negative thermal expansion behaviors[12, 13], NZP-like frameworks were chosen for In(I) ion exchange.

The $NaZr_2(PO_4)_3$ (NZP) structure consists of corner-sharing ZrO_6 octahedra and PO_4 tetrahedra arranged so that there is a three-dimensional channel system running through the material. There are three distinct types of sites in the NZP channel system that could contain exchangeable cations. However, in NZP itself, only the octahedrally coordinated site is occupied.

The current work reports the preparation, crystal structure and thermal properties of $InZr_2(PO_4)_3$. The crystal chemistry of In(I) in this material is compared with that of other univalent cations in similar hosts.

4.2 Synthesis of $InZr_2(PO_4)_3$

$InZr_2(PO_4)_3$ was first prepared by ion exchange reaction starting from $AgZr_2(PO_4)_3$[14-16] by Hakan Arslan during his work in Dr. Wilkinson's group. According to Hakan's procedure, $AgZr_2(PO_4)_3$ was sealed into an evacuated silica tube with indium and iodine in a 1:20:10 molar ratio. The tube was heated at 1°C/min to 500 °C and annealed at 500 °C for 120h. After cooling the sample down to room temperature, the tube was broken open. The sample was treated with 0.3 M HCl at 95°C. After hydrogen evolution was complete it was recovered by filtration and washed with hot distilled water. The recovered sample was dried overnight at 75 °C. Powder X-ray diffraction data, elemental and thermogravimetric analyses confirmed the recovered product to be $InZr_2(PO_4)_3$.

However, in my hands repeating the same procedure did not give the same product. The procedure was modified and the product synthesized from the new procedure was confirmed to be $InZr_2(PO_4)_3$ by thermogravimetric analysis, powder X-ray diffraction and X-ray fluorescence spectroscopy.

$InZr_2(PO_4)_3$ was prepared by ion exchange starting from $AgZr_2(PO_4)_3$. The latter was synthesized from stoichiometric amounts of Ag_2CO_3, ZrO_2, and $(NH_4)H_2PO_4$. The reactants were ground and initially heated to 600 °C for 6 hours and then heated to 1100°C for 48 hours. The sample was removed from the furnace, ground and reheated to

1200°C for another 48 hours. The product was confirmed to be pure single phase $AgZr_2(PO_4)_3$ (Figure 4.1.).

$AgZr_2(PO_4)_3$, indium metal and iodine was sealed in an evacuated quartz ampoule in a 1:13:3 molar ratio. The mixture was heated at 1 °C/min to 400 °C and annealed for 120 hours, after which it was broken open and the sample was treated with 15% HCl. After hydrogen evolution was complete, the product was recovered by filtration and washed with hot distilled water. The recovered sample, which was off-white, was dried overnight at 75 °C.

Powder X-ray diffraction data for the product was recorded using a Scintag X1 diffractometer equipped with Peltier cooled solid state detector. Data was collected, in steps of 0.02°, over the range 5-140° 2θ. High temperature powder X-ray diffraction data under nitrogen at temperature up to 500 °C were collected with an X'Pert PRO MPD diffractometer from PANalytical equipped with an Anton-Paar HTK1200 high-temperature stage and a scintillation point detector at the X-ray Analysis Group, Materials Science and Engineering at Georgia Institute of Technology. Additionally, the data under a $4\%H_2/96\%N_2$ mixture were collected with Philips X'Pert PRO MPD powder X-ray diffractometer equipped with an X'Celerator "Real-Time Multiple Strip" detector and an Anton-Paar XRK900 high-temperature stage at the High Temperature Materials Laboratory at Oak ridge National Laboratory. High temperature synchrotron data were also collected at the Advanced Photon Source, Argonne National Laboratory.

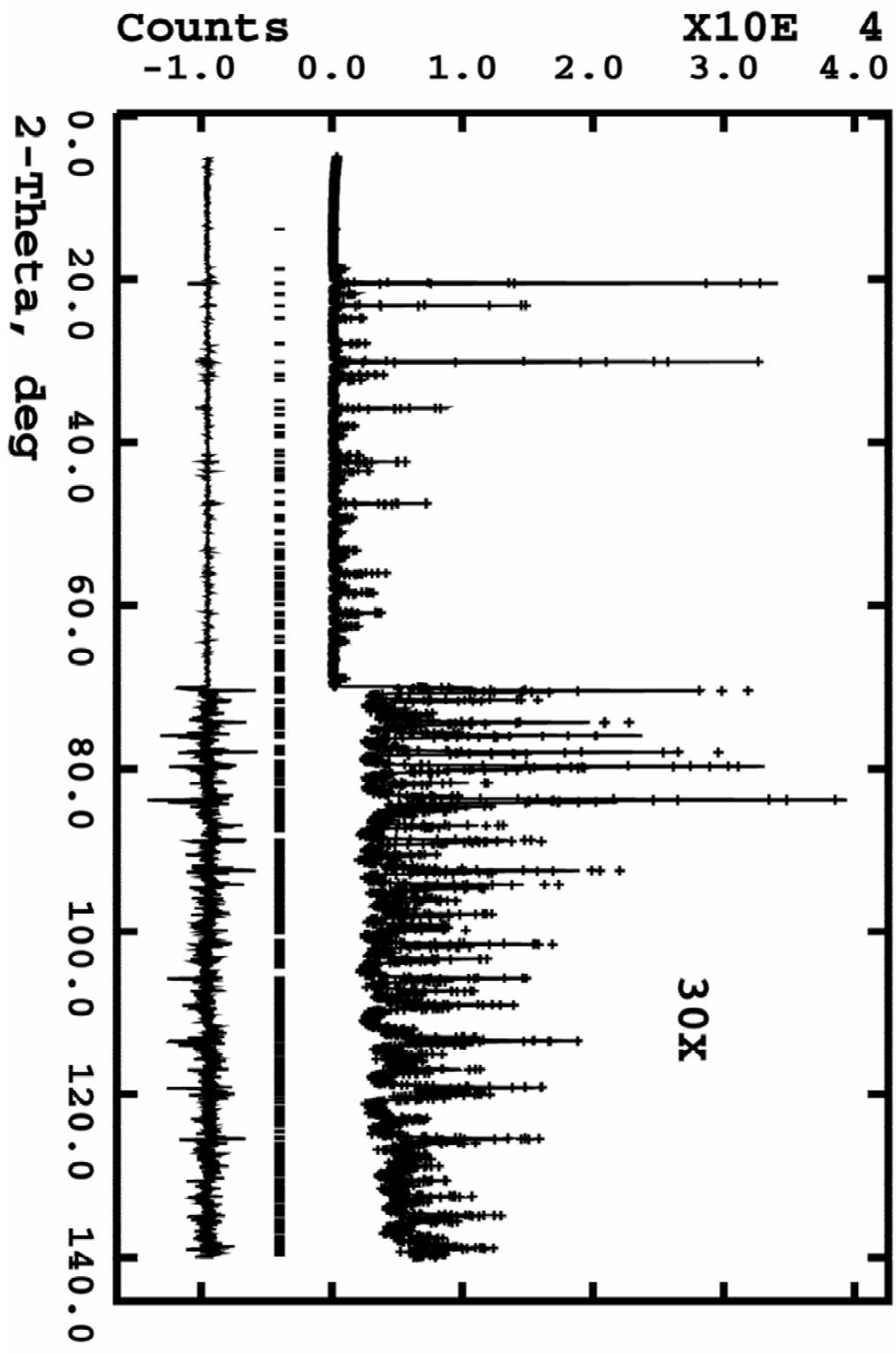

Figure 4.1: Rietveld refinement of the $AgZr_2(PO_4)_3$ structural model fitted to X-ray powder diffraction data.

4.3. Results and Discussion

4.3.1 Chemical, Thermogravimetric, and X-ray Fluorescence Analyses, and Ex-Situ Powder X-ray Diffraction

Chemical analysis of $InZr_2(PO_4)_3$ synthesized by Hakan shows that it contains 31.13% zirconium and 20.72% indium, which compare well with the values expected for $InZr_2(PO_4)_3$ (31.33% Zr and 19.72% In). The TGA experiment in air shows that the material is stable towards oxidation up to 400 °C. The majority of the weight gain occurs above 550 °C, and it is complete by 650 °C. The observed weight gain of 2.55% between 400 and 650 °C is consistent with the oxidation of all the In(I) in $InZr_2(PO_4)_3$ to In(III) (expected weight gain 2.74%).

Powder X-ray diffraction data for $InZr_2(PO_4)_3$ synthesized using the second procedure were collected. A Rietveld refinement of the $InZr_2(PO_4)_3$ structure was carried out using Wilkinson's model for $GaZr_2(PO_4)_3$[17] as a starting point. Isotropic temperature factors were employed for all atoms except indium. The crystallographic details are summarized in Table 4.1, the final coordinates and temperature factors from this refinement are reported in Table 4.2, some selected distances are given in Table 4.3., and the final profile fit is shown in Figure 4.2. The coordination environment of In(I) in $InZr_2(PO_4)_3$ is like that found in the alkali metal zirconium phosphates, with six oxygens all at the same distance from the cation, and the unit cell constants for $InZr_2(PO_4)_3$ are close to those for $RbZr_2(PO_4)_3$.

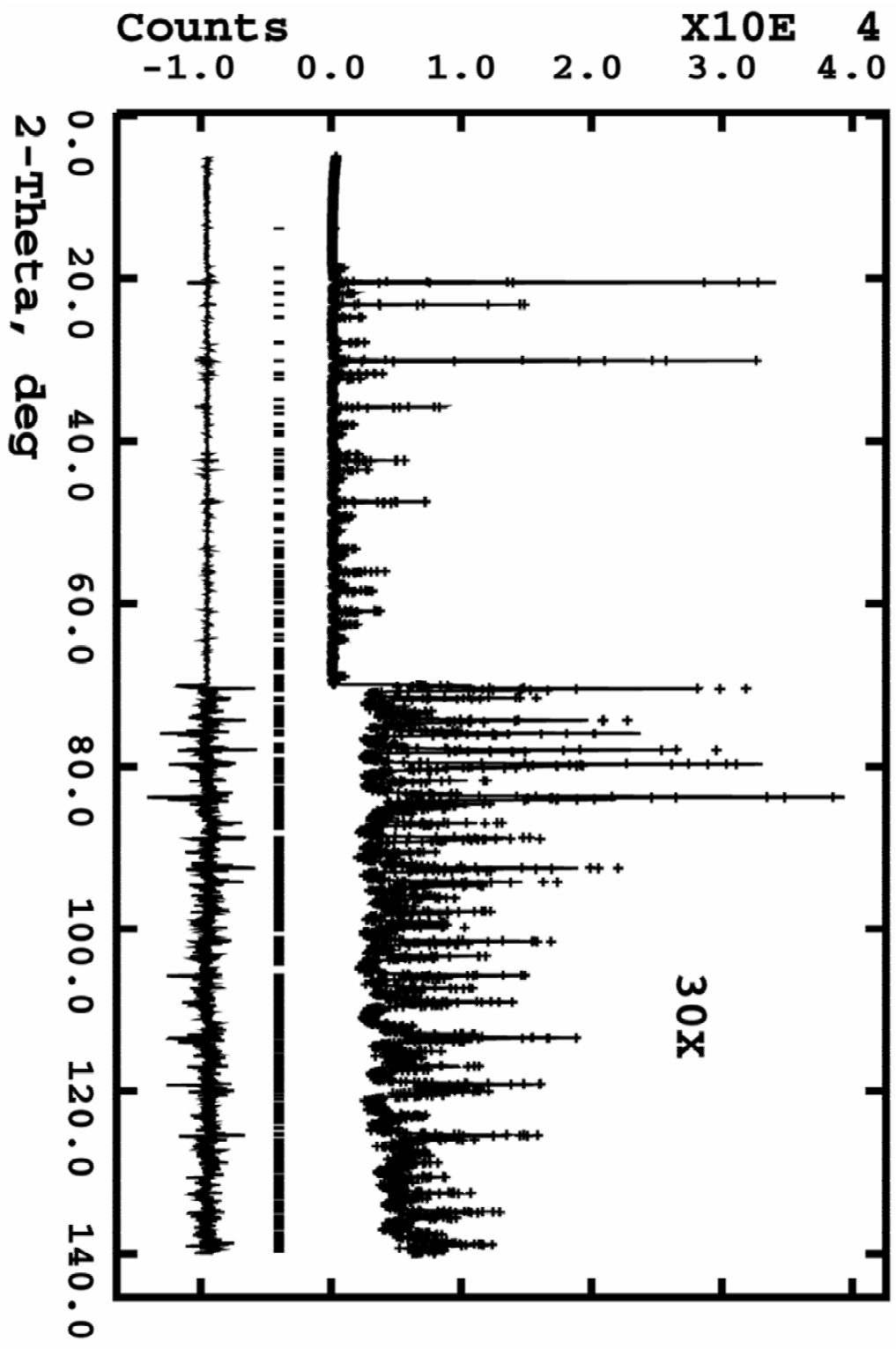

Figure 4.2: Rietveld refinement of the $InZr_2(PO_4)_3$ structural model fitted to powder X-ray diffraction data.

Table 4.1: Summary of Crystal Data and Structure Refinement Details for $InZr_2(PO_4)_3$

space group	R-3c
x-ray wavelength/Å	1.5405
T/K	296
Fw	582.17
a/Å	8.67114(5)
c/Å	24.3467(2)
V/Å^3	1585.34(2)
Z	6
ρ_x/g cm^{-3}	3.659
Color	off-white
abs corr	none required (flat-plate reflection geometry)
angular range (2θ)/deg	5.000-139.980
No. of data points	6749
No. of refls	706
No. of refined params	33
R_{wp}/%	10.61 8.86[a]
R_p/%	7.42 6.7[a]
χ^2	3.777
R_F2/%	4.71[a]

[a] $R_{wp} = \sum w(y_{io} - y_{ic})^2/\sum w(y_{io})^2$ (weights based on counting statistics); $R_p = \sum(y_{io} - y_{ic})^2/\sum(y_{io})^2$; $R_F2 = [\sum(F_o^2 - F_c^2)^2/\sum(F_o^2)^2]^{1/2}$ (F_o is estimated from the profile and may be biased by the model).

Table 4.2: Refined Structural Parameters for $InZr_2(PO_4)_3$

atom	x	y	z	10^2U_{11}[a]	10^2U_{22}
Zr	0	0	0.15112(4)	0.26(3)	
P	0.2861(3)	0	0.25	0.30(6)	
O	0.1635(5))	0.0511(6)	0.2004(1)	0.5(1)	
O	0.2006(5)	0.1759(5)	0.0990(2)	0.8(1)	
In	0	0	0	4.58(7)	1.85(8)

[a] Isotropic temperature factor or U_{11} if an anisotropic temperature factor was refined.
[b] $U_{11} = U_{22}$, $U_{12} = 0.5U_{11}$, and $U_{13} = U_{23} = 0$.

Table 4.3: Selected Distances (Å) for $InZr_2(PO_4)_3$

In(1)-O(2)	6x	2.916(4)	P(1)-O(1)	2x	1.521(4)
Zr(1)-O(1)	3x	2.070(4)	P(1)-O(2)	2x	1.520(4)
Zr(1)-O(2)	3x	2.077(4)			

Fluorescence X-ray analysis showed a similar In/Zr peak ratio for both Hakan's sample and the new sample (0.56 and 0.57, respectively). The TGA experiment in air also showed similar behavior. However, as the baseline was not corrected a negative slope was observed. The material is stable towards oxidation up to 400 °C. The majority of the weight gain occurs above 550 °C, and it was complete by 700 °C. The observed weight gain of 2.89% between 400 and 650 °C is consistent with the oxidation of all the In(I) in $InZr_2(PO_4)_3$ to In(III) (expected weight gain 2.74%) (Figure 4.3)

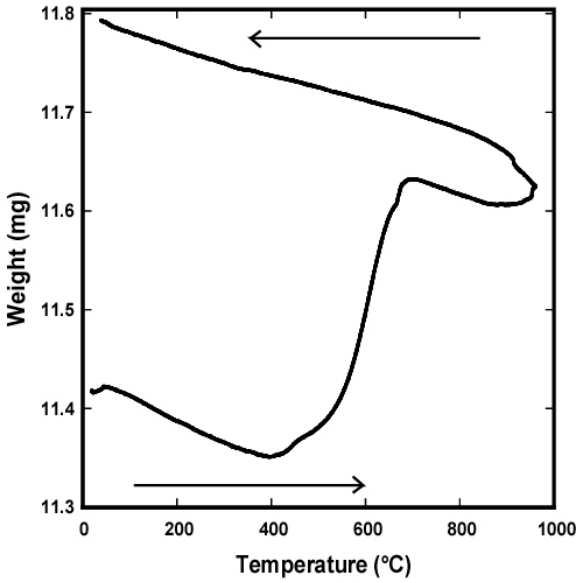

Figure 4.3: Thermogravimetric analysis of $InZr_2(PO_4)_3$ under air.

4.3.2 In-Situ High Temperature Diffraction Experiments

4.3.2.1 Experiments Under Nitrogen

High temperature powder X-ray diffraction data under nitrogen up to 500 ^oC were collected with the PANalytical instrument at the Materials Science and Engineering at Georgia Institute of Technology. However, it is believed that there was water in the

system during the data collection because of an incident prior to the experiment. Therefore, the atmosphere of the experiment should be considered as humid nitrogen.

It was observed that either decomposition, oxidation or a reaction with water starts at around 400 ^{o}C (Figure 4.3). The change in the sample is obvious from the diffraction patterns starting from 450 ^{o}C. However, plots of the cell parameters as a function of temperature indicate that the change starts earlier, around 400 ^{o}C (Figure 4.4). Material shows negative thermal expansion and it should also be noted that it continues to shrink even after the change in the unit cell parameters (Figure 4.5).

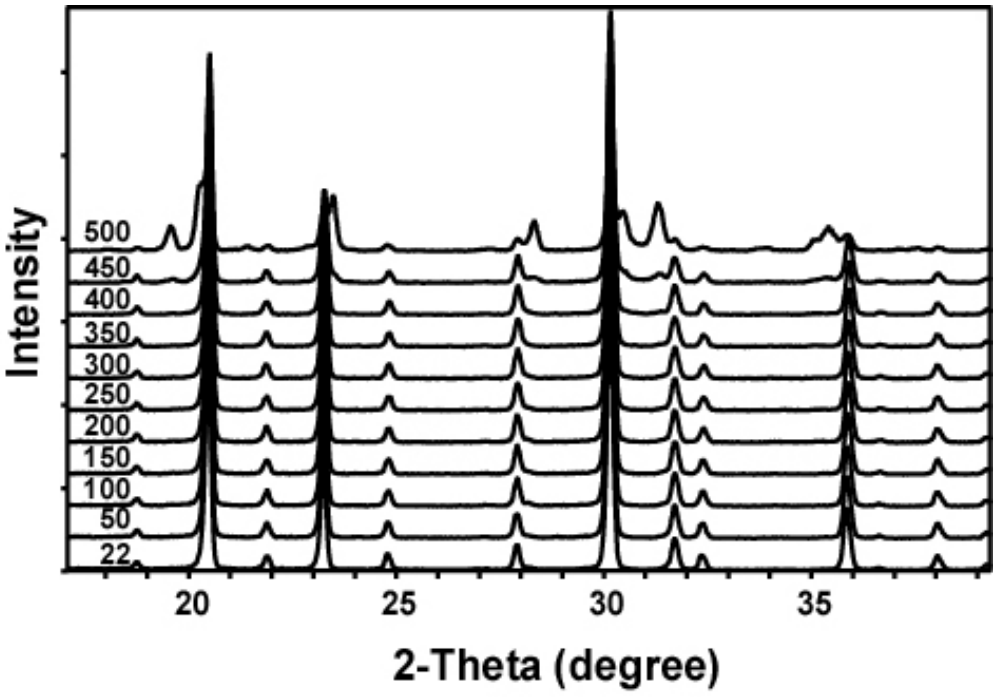

Figure 4.4**:** High temperature x-ray powder diffraction patterns of $InZr_2(PO_4)_3$. It is obvious that the sample is changing above 400 ^{o}C.

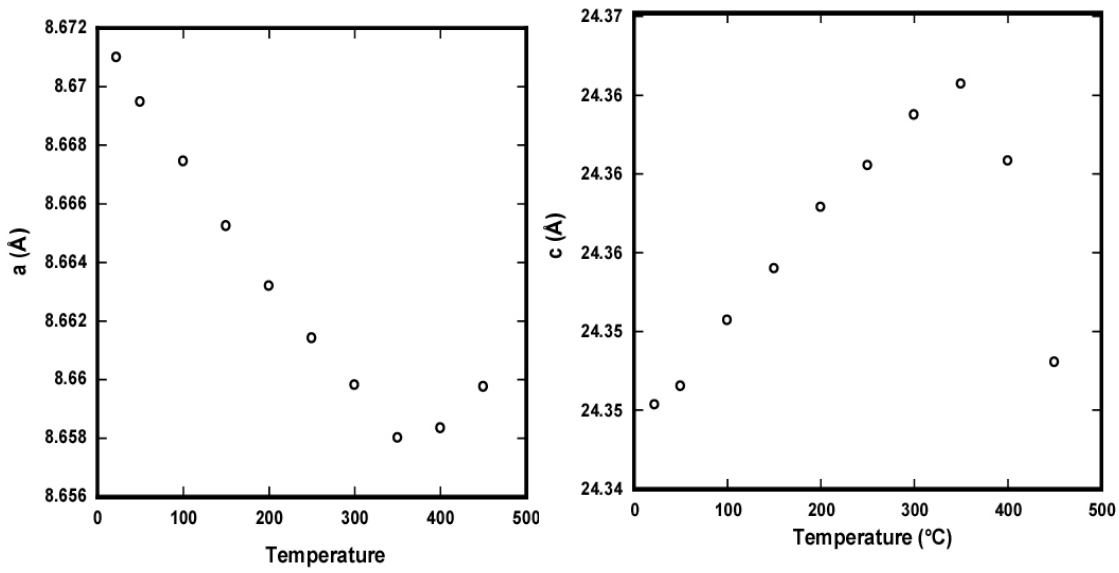

Figure 4.5: Cell parameters, a (Left) and c (Right), as a function of temperature for $InZr_2(PO_4)_3$. Experiment in nitrogen atmosphere.

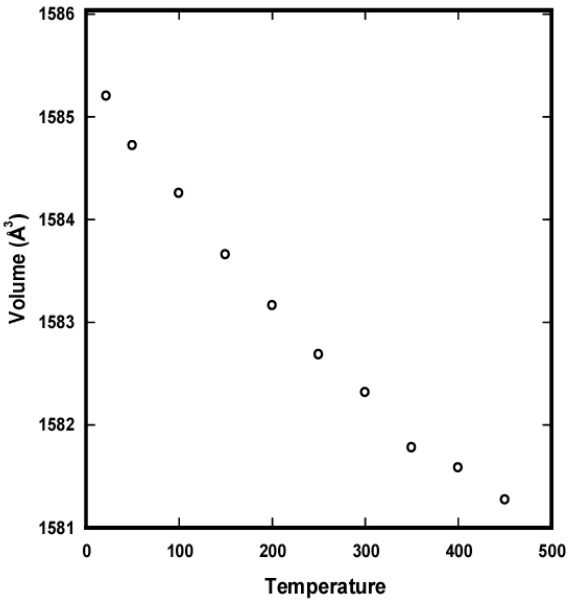

Figure 4.6: Unit cell volume as a function of temperature for $InZr_2(PO_4)_3$. Experiment in nitrogen atmosphere.

4.3.2.2 Experiments Under 4%H_2/96%N_2 Mixture

As we had previously had problems achieving a non-oxidizing atmosphere using the instrument in the Materials Science Engineering Department at Georgia Institute of Technology, further variable temperature data were collected at the High Temperature Materials Laboratory, Oak Ridge National Laboratory. The data were collected under reducing atmosphere, 4% H_2/96%N_2 mixture, to prevent oxidation. During heating, data were collected at room temperature and then at 50 ^oC intervals up to 900 ^oC starting from 50 ^oC. In addition, during cooling data were collected at 200 ^oC intervals down to 300 ^oC and then at room temperature. Plots of the unit cell volume as a function of temperature confirm that the material is a negative thermal expansion material. However, the cell parameters on heating and cooling do not match. This was also observed for $GaZr_2(PO_4)_3$.

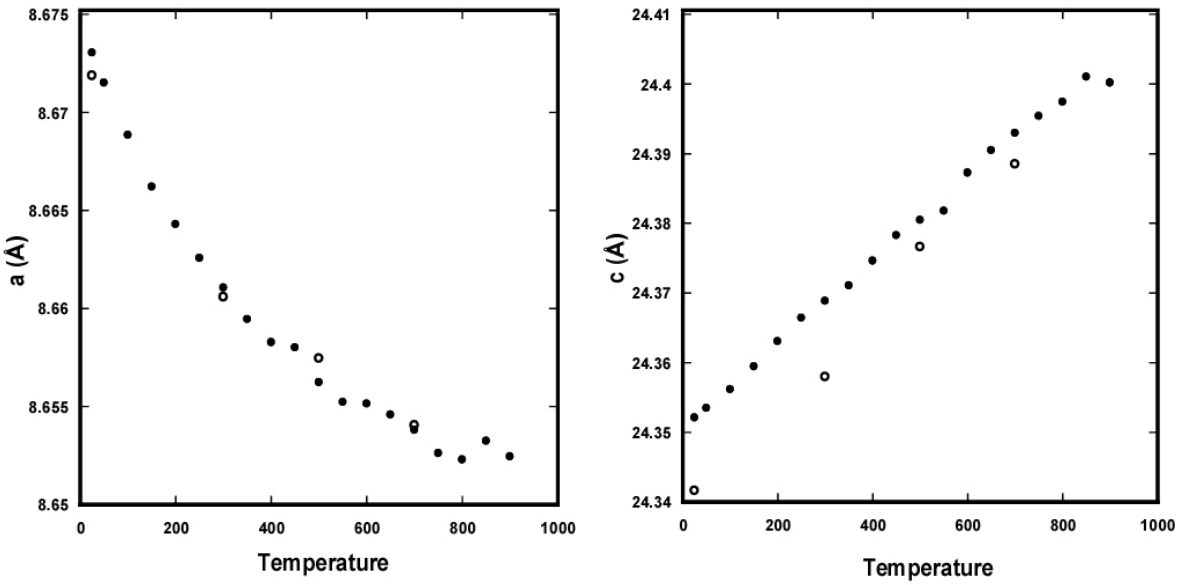

Figure 4.7: Cell parameters, a (left) and c (right), as a function of temperature for $InZr_2(PO_4)_3$. Experiment in H_2/N_2 mixture. Solid circles: during heating; Open circles: during cooling.

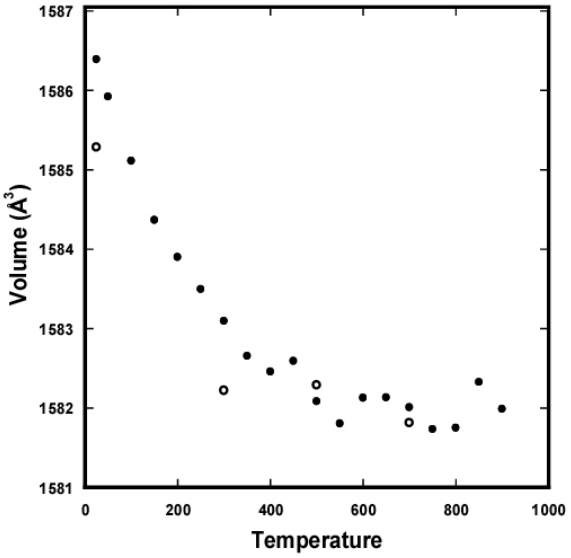

Figure 4.8: Unit cell volume as a function of temperature for $InZr_2(PO_4)_3$. Experiment in H_2/N_2 mixture. Solid circles: during heating; Open circles: during cooling.

4.3.2.3 Experiment Under Low Vacuum Using Synchrotron Radiation

Further experiments to confirm the behavior of the material were performed using synchrotron radiation at the Advanced Photon Source (APS) at Argonne National Laboratory (ANL). Experimental conditions and the temperature program were same as the $GaZr_2(PO_4)_3$ experiment that was explained in Sections 3.3.2.3. The pressure was between $4.2x10^{-3}$ and $1.1x10^{-3}$ Torr and because of the limited beam time better vacuum conditions could not be obtained.

Structural parameters could only be refined up to 450 ^oC. It is believed that the sample is oxidized because of the low vacuum conditions. Results are very similar with the experiment under nitrogen in the MSE department; a decreases and c increases below 400 ^oC. In addition, they do the opposite above 400 ^oC (Figures 4.7 and 4.8).

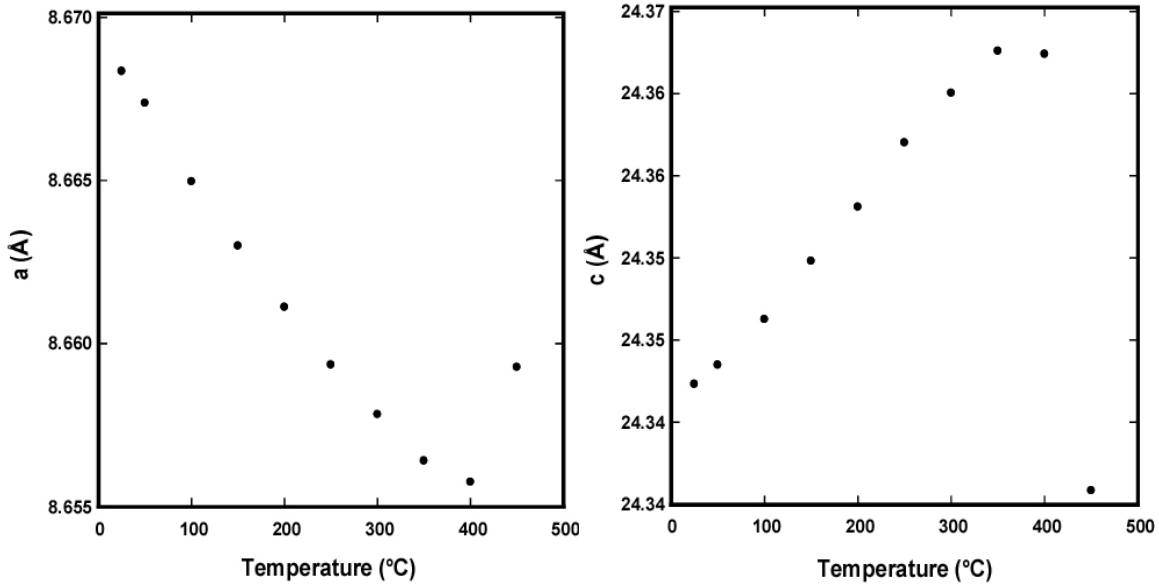

Figure 4.9: The unit cell parameters, a (Left) and c (Right), as a function of temperature for $InZr_2(PO_4)_3$. Data collected under low vacuum at APS.

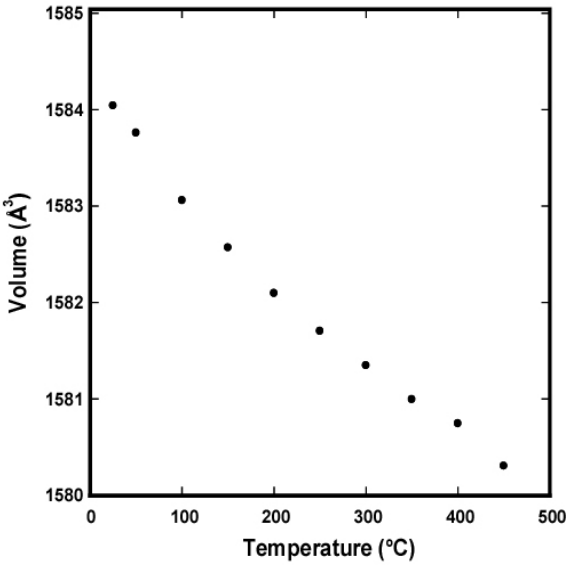

Figure 4.10: Unit cell volume as a function of temperature for $InZr_2(PO_4)_3$. Data collected under low vacuum at APS

4.4 Conclusion and Outlook

Comparison of the data collected using equipment in the Materials Science Engineering Department (MSE) at the Georgia Institute of Technology, High Temperature Materials Laboratory (HTML) at Oak Ridge National Laboratory and at the Advanced Photon Source (APS) at Argonne National Laboratory confirms that the behavior observed at MSE and APS is the oxidation of the sample (Figures 4.11 and 4.12). These results show that the issue is very similar with $GaZr_2(PO_4)_3$ explained in Chapter 3.

The decomposition temperature in an inert atmosphere should be determined. Evacuated closed system experiments such as those in Section 3.3.3.2 can be repeated below decomposition temperature to see if the sample changes. TG data can be collected for a very long time at a constant temperature to see if there is any evaporation from the sample under inert atmosphere.

Ionic conductivity of the material should be measured for possible applications.

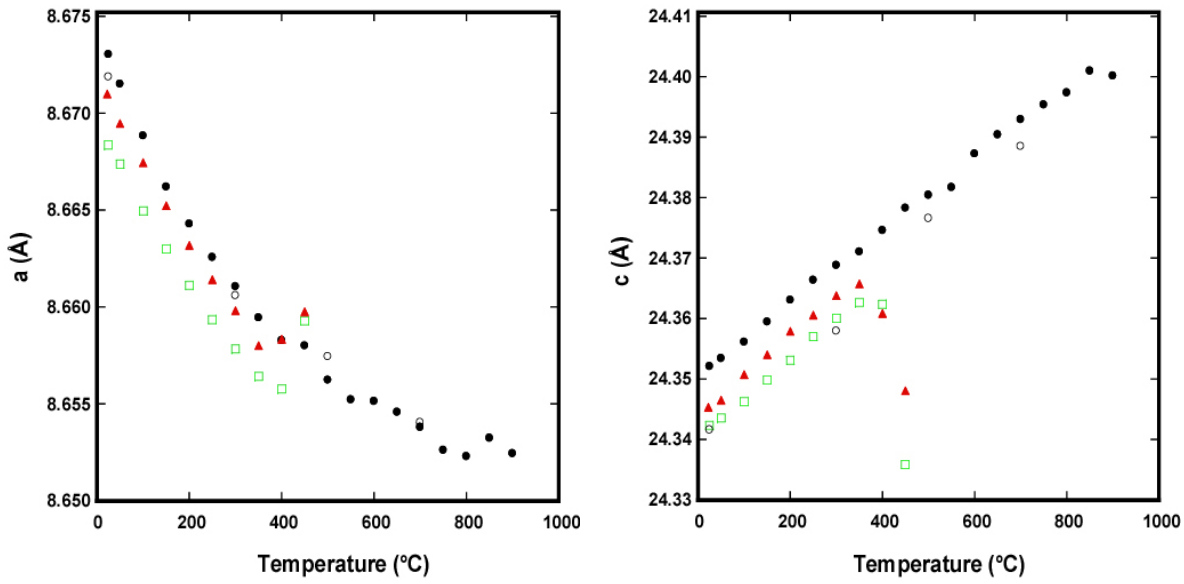

Figure 4.11: The unit cell parameters a (Right) and c (Left), as a function of temperature for $InZr_2(PO_4)_3$. Data collected under low vacuum at APS: Green rectangles. Data collected under H_2/N_2 mixture at ORNL: Solid black circles: on heating; Open black circles: on cooling. Data collected under nitrogen at MSE: Red triangles.

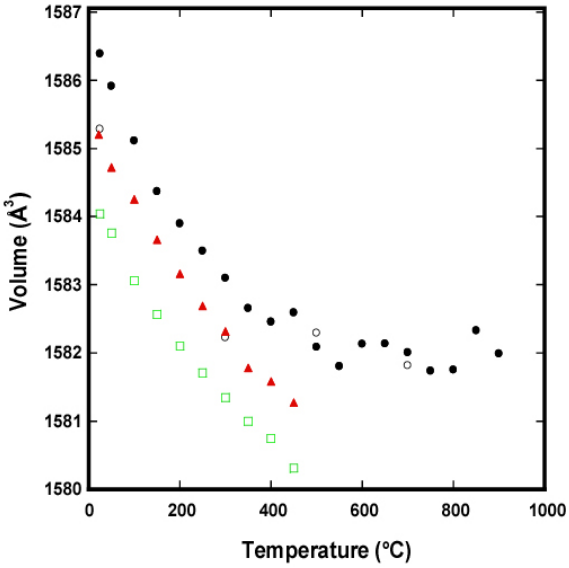

Figure 4.12: Unit cell volume as a function of temperature for $InZr_2(PO_4)_3$. Data collected under low vacuum at APS: Green rectangles. Data collected under H_2/N_2 mixture at ORNL: Solid black circles: on heating; Open black circles: on cooling. Data collected under nitrogen at MSE: Red triangles.

4.5 References

1. Dronskowski, R., $InFeBr_3$ and $InMnBr_3$: Synthesis, Crystal Structure, Magnetic Properties, and Electronic Structure. *Inorganic Chemistry* **1994,** 33, 5927-5933.

2. Schmidbaur, H., Arene Complexes of Univalent Gallium, Indium, and Thallium. *Angewandte Chemie, International Edition in English* **1985,** 24, 893-904.

3. Tuck, D. G., The Lower Oxidation States of Indium. *Chemical Society Reviews* **1993**, 269-276.

4. Hinchcliffe, A. J.; Ogden, J. S., Matrix Isolation Studies of the Gallium-Indium-Oxygen System. Infrared Spectra and Structures of Molecular Ga_2O, In_2O and InOGa. *Journal of Physical Chemistry* **1973,** 77, 2537-2544.

5. Lakin, N. M.; van der Hoek, G.; Beattie, I. R.; Brown, J. M., The identification of In_2O in the gas phase by high resolution electronic spectroscopy. *Journal of Chemical Physics* **1997,** 107, 4439-4442.

6. Kikuchi, E.; Ogura, M.; Aratani, N.; Sugiura, Y.; Hiromoto, S.; Yogo, K., Promotive effect of additives to In/H-ZSM-5 catalyst for selective reduction of nitric oxide with methane in the presence of water vapor. *Catalysis Today* **1996,** 27, (1-2), 35-40.

7. Hart, V. I.; Bryant, M. B.; Butler, L. G.; Wu, X.; Dooley, K. M., Proton-poor, gallium- and indium-loaded zeolite dehydrogenation catalysts. *Catalysis Letters* **1998,** 53, (1-2), 111-118.

8. Swanson, A. B.; Anderson, J. S., Indium Tungsten Bronze. *Materials Research Bulletin* **1968,** 3, 149-152.

9. Pitt, M. G.; Fray, D. J., The Preparation and Physical Properties of Indium β-Alumina Single Crystals. *Journal of Solid State Chemistry* **1982,** 43, 227-236.

10. Pitt, M. G.; Fray, D. J., Electrical Properties of Indium and Gallium Beta Alumina. *Electrochimica Acta* **1982,** 27, 15-24.

11. Thauern, H.; Glaum, R., Contributions on crystal chemistry and thermal behaviour of anhydrous phosphates. XXXIII. In2P2O7 an Indium(I)-

diphosphatoindate(III), and In-4(P2O7)(3) - Synthesis, crystallization, and crystal structure. *Zeitschrift Fur Anorganische Und Allgemeine Chemie* **2003,** 629, (3), 479-486.

12. Boilot, J. P.; Collin, G.; Colomban, P., Relation Structure-Fast Ion Conduction in the NASICON solid Solution. *Journal of Solid State Chemistry* **1988,** 73, 160-171.

13. Alamo, J., Chemistry and properties of solids with the [NZP] skeleton. *Solid State Ionics* **1993,** 63-65, 547-561.

14. Winand, J.-M.; Rulmont, A.; Tarte, P., Synthesis amnd Study of New Compounds $(M^{I})(N^{IV})_2(PO_4)_3$ with NASICON-Like Structure (M = Ag, Cu; N = Ge, Hf, Sn, Ti, Zr). *Journal of Solid State Chemistry* **1993,** 107, 356-361.

15. Barj, M.; Perthuis, H.; Colomban, P., Domaines D'existence, Disotrtions Structurales et Modes de Vibration des Ions Conducteurs dnas les Reseaux Hotes de Type NASICON. *Solid State Ionics* **1983,** 11, 157-177.

16. Angenault, J.; Couturier, J. C.; Quarton, M., Conductivitie Ioniques des Solutions Solides $Ag_{1+x}Zr_{2-x}M_x(PO_4)_3$. *Materials Research Bulletin* **1989,** 24, 789-794.

17. Wilkinson, A. P., Crystal Chemistry of Ga(I) in Oxides: Ga^{+}-β"-Alumina and $GaZr_2(PO_4)_3$. *Inorganic Chemistry* **1997,** 36, 1602-1607.

CHAPTER 5

SYNTHESIS AND CHARACTERIZATION OF $M[Zr_{2-x}Ti_x](PO_4)_3$ (M=Ag, Ga) SOLID SOLUTIONS

5.1 Introduction

Initially, the preparation of $GaTi_2(PO_4)_3$ was attempted using the procedure that had worked of $GaZr_2(PO_4)_3$ so that their thermophysical properties could be compared. However, many attempts to synthesize the compound using with different temperatures and annealing times failed. It was also observed from the cell and occupational parameters extracted from Rietveld refinements that there was no Ga(I) exchange. Therefore, it was decided to prepare solid solutions $Ag[Zr_{2-x}Ti_x](PO_4)_3$ ($0 < x < 2$) and ion exchange them with Ga(I) in order to better understand the ion exchange limitations and the effects of introducing Ga(I) into the solid solutions' structures.

5.2 Experimental and Results

5.2.1 Synthesis of $Ag[Zr_{2-x}Ti_x](PO_4)_3$ solid solutions

Solid solutions of $Ag[Zr_{2-x}Ti_x](PO_4)_3$ ($x = 0.25, 0.5, 0.75, 1, 1.25, 1.5, 1.75$) were prepared from stoichiometric amounts of Ag_2CO_3, ZrO_2, TiO_2 and $NH_4H_2(PO_4)_3$. Mixed reactants were first heated to 600 ^oC for 6 hours and then to 1100 ^oC for 48 hours after which they were removed from the furnace. The resulting samples were ground and reheated to 1200 ^oC for 48 hours. Powder X-ray diffraction patterns of the final products were recorded and structural models for each sample were Rietveld refined. The quality

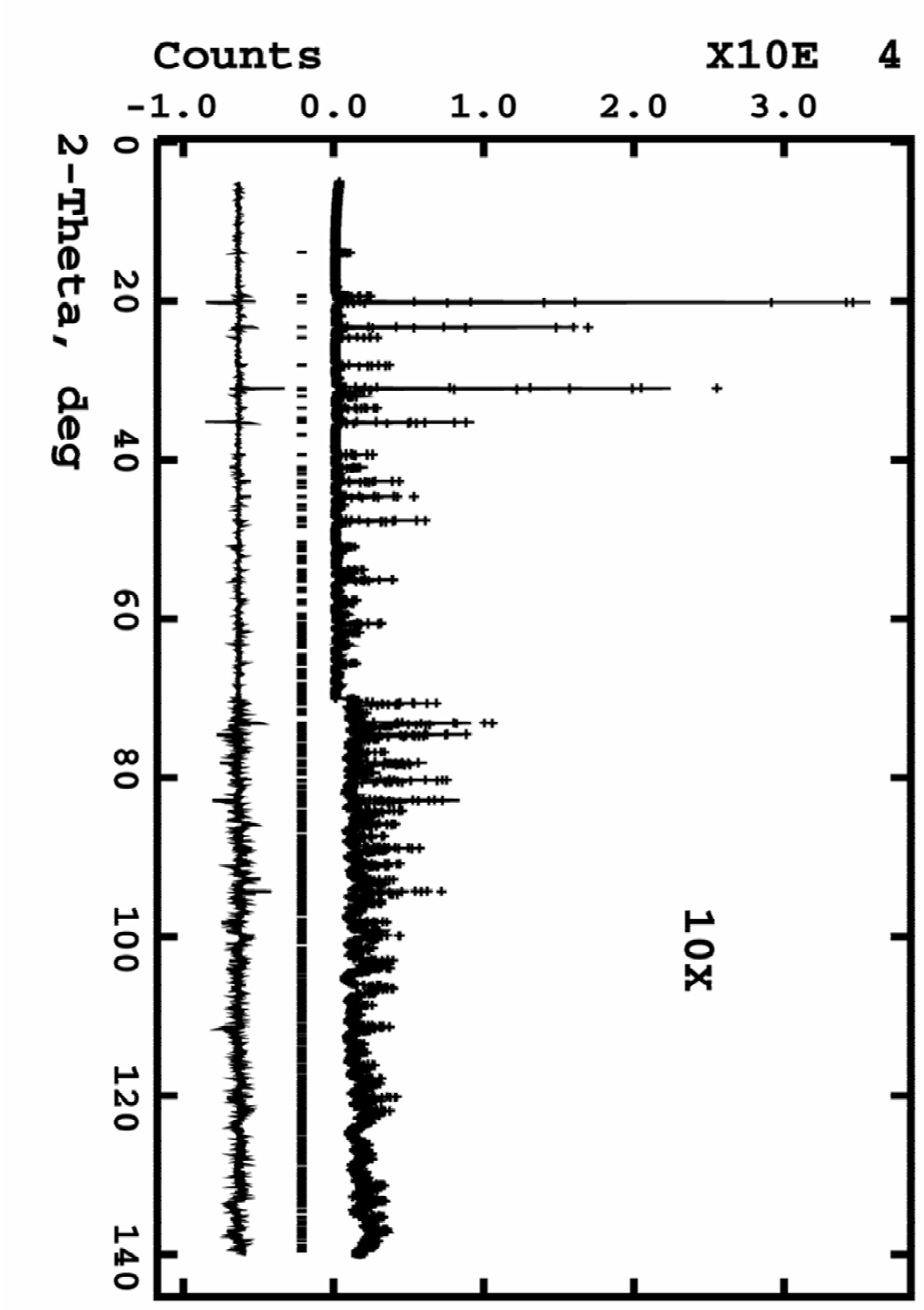

Figure 5.1: Rietveld fit to the powder X-ray diffraction data for $AgZr_2(PO_4)_3$

of the samples were very good. A Rietveld fit to the powder X-ray diffraction data for $AgZr_2(PO_4)_3$ is shown in Figure 5.1 as an example.

The cell parameters and volume as a function of x were plotted. Cell parameters, a and c, linearly decrease as a bigger ion, Zr^{4+}, was substituted by a smaller one, Ti^{4+} (Figure 5.2).

5.2.2 Ion exchange reactions of $Ag[Zr_{2-x}Ti_x](PO_4)_3$ solid solutions with Ga(I)

Each solid solution sample was sealed into an evacuated quartz ampoule with gallium metal and iodine in a 1:13:3 molar ratio. The tubes were heated to 300 ^oC and annealed for 72 hours, after which they were cooled down to room temperature and broken open. Each sample was treated with 6 M of HCl until the hydrogen gas evolution was over. The resulting products were filtered, washed with distilled water and dried at 60 ^oC for 2 hours.

Powder X-ray diffraction patterns of the samples were recorded and structural models for the samples were Rietveld refined. Initially, it was expected that the ratio of Ga(I) to Ag(I) in the solid solutions would follow a smooth trend; increasing with decreasing x. However, the fractional occupancy parameters of Ga(I) and Ag(I) in the M(I) site do not vary smoothly (Table 5.1). The cell parameters, a and c, as a function of composition also show that solid solutions with $x > 1.25$ and $x < 1.00$ behave differently. Above $x = 1.25$ there is almost zero Ga(I) in the samples. However below $x = 1$, there is an abrupt change in the unit cell parameters which indicates that the material ion exchanged (Figure 5.2).

Table 5.1: Fractional occupancies of the ions in the M(I) site of $M[Zr_{2-x}Ti_x](PO_4)_3$.

X	Ga(I)	Ag(I)
0.25	1.32(1)	-0.32(1)
0.5	1.01(2)	-0.01(2)
0.75	1.02(1)	-0.02(1)
1.0	1.630(7)	-0.630(7)
1.25	0.87(1)	0.13(1)
1.5	0.35(1)	0.64(1)
1.75	-0.25(3)	1.25(3)
2.0	0.02(1)	0.976(1)

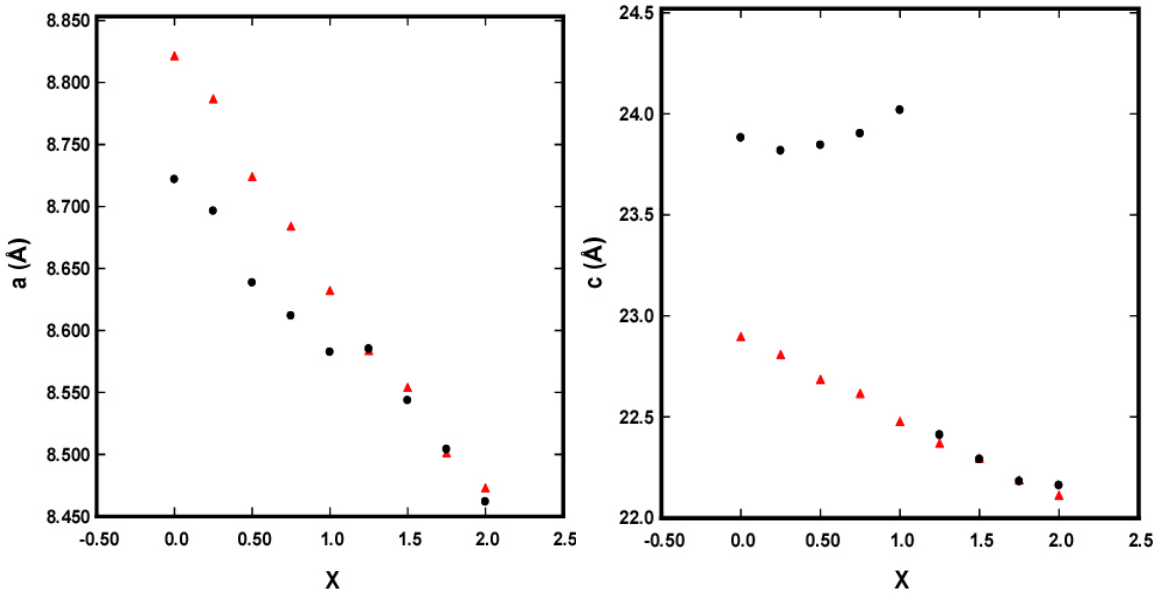

Figure 5.2: Unit cell parameters a (Left) and c (Right) as a function of composition. Red triangles: $Ag[Zr_{2-x}Ti_x](PO_4)_3$; Black circles: Solid solutions after ion exchange with Ga.

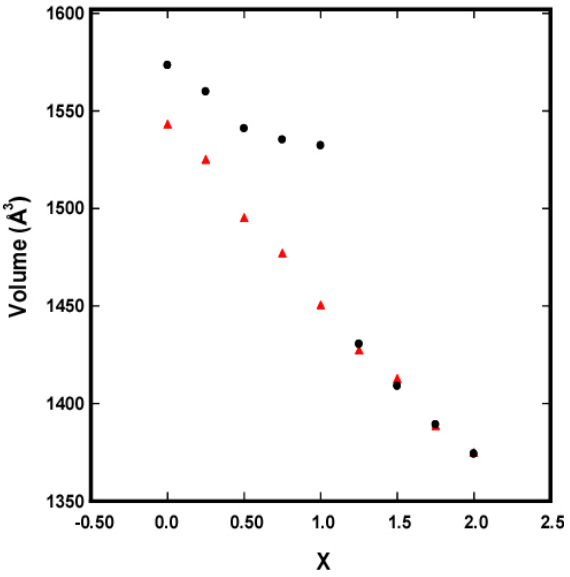

Figure 5.3: Unit cell volume as a function of composition. Red triangles: $Ag[Zr_{2-x}Ti_x](PO_4)_3$; Black circles: Solid solutions after ion exchange with Ga.

All the $Ag[Zr_{2-x}Ti_x](PO_4)_3$ solid solution samples crystallize in space group R -3 c at room temperature. However, there may be differences at the temperature, 300 ^oC, where the ion exchange reactions were performed. Therefore, it was decided to collect in-situ powder X-ray diffraction data at high temperatures to see if the unexpected ion exchange behavior was associated with a structural change on going for $x < 1$ to $x > 1.25$ at 300 ^oC.

5.2.3 In-Situ High Temperature Diffraction Experiments

High temperature powder X-ray diffraction data were recorded with a Philips X'Pert PRO MPD powder X-ray diffractometer equipped with an Anton-Paar XRK900 high-temperature stage at the High Temperature Materials Laboratory (HTML) at Oak Ridge National Laboratory (ORNL).

One solid solution composition from each side of the break point, $Ag[Ti_{1.5}Zr_{0.5}](PO_4)_3$ and $Ag[TiZr](PO_4)_3$, were chosen. In addition, high temperature powder X-ray diffraction data for $AgZr_2(PO_4)_3$ were also recorded as there was no literature on it.

The experiments were carried out under air. On heating, data were collected at room temperature and at 50 ^oC intervals starting from 50 ^oC up to 900 ^oC. On cooling, data were collected at 200 ^oC intervals down to 300 ^oC and then at room temperature. The behavior of all the parameters is non-linear (Figure 5.3). The data were fitted to the polynomial equation (1) and the coefficients of thermal expansion are calculated using the equation (2), where the coefficient of thermal expansion is: $\alpha = 1/p\ dP/dT$.

$$p = p_2T^2 + p_1T + p_0 \qquad (1)$$

$$\alpha = \frac{p_1 + 2p_2T}{p} \qquad (2)$$

Experimentally determined polynomial parameters are tabulated in Table 5.2, the coefficients of thermal expansion for each material are tabulated in Tables 5.3, 5.4 and 5.5, and the average coefficients of thermal expansion are shown in Table 5.6.

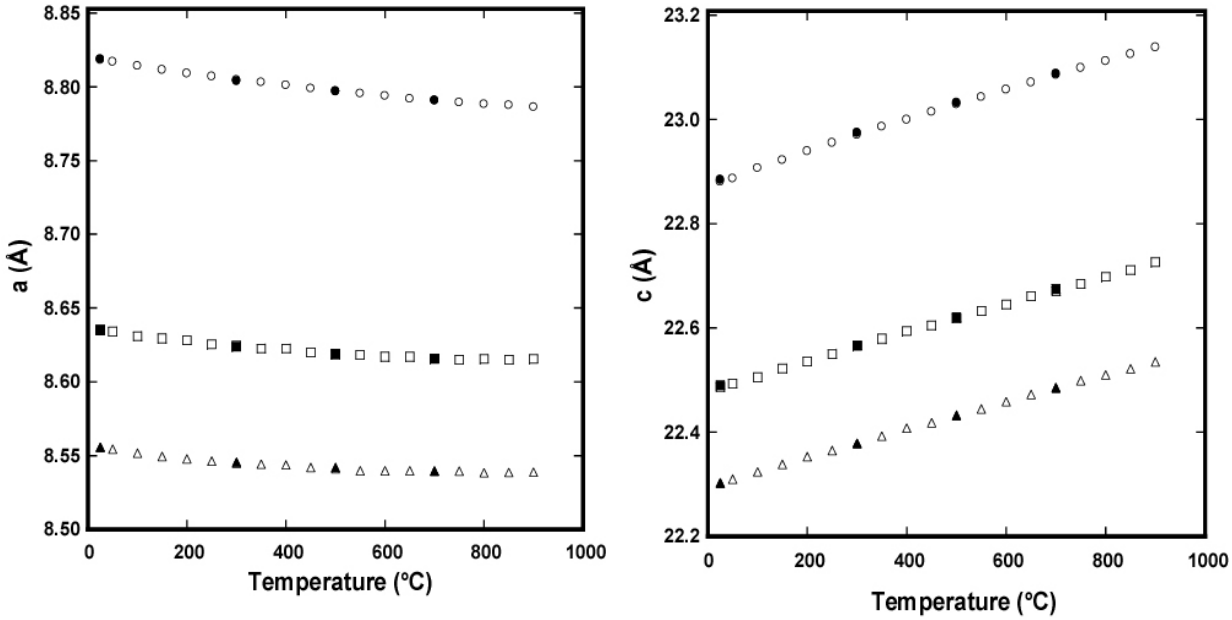

Figure 5.4: Unit cell parameters, a and c, with temperature. Experiments in air. Circles : $AgZr_2(PO_4)_3$; Rectangles : $Ag[TiZr](PO_4)_3$; Triangles : $Ag[Ti_{1.5}Zr_{0.5}](PO_4)_3$. Open symbols: heating; Solid symbols: cooling.

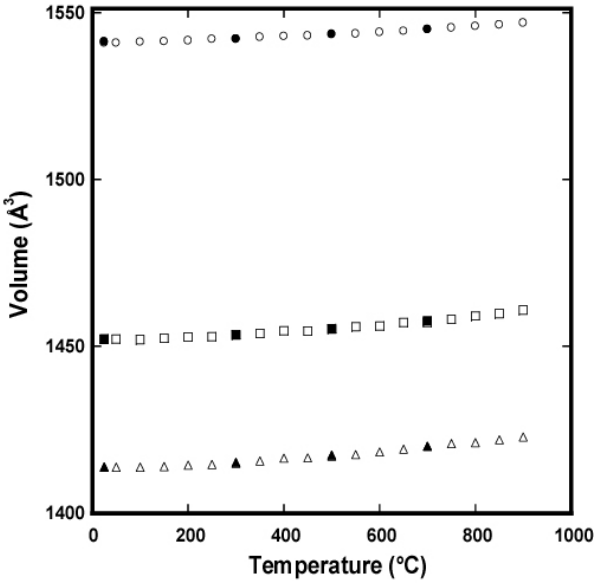

Figure 5.5: Unit cell volume with temperature. Circles : $AgZr_2(PO_4)_3$; Rectangles : $Ag[TiZr](PO_4)_3$; Triangles : $Ag[Ti_{1.5}Zr_{0.5}](PO_4)_3$. Open symbols: heating; Solid symbols: cooling.

Table 5.2: Experimentally determined polynomial parameters

Material	Axis	p_2	p_1	p_0
$AgZr_2(PO_4)_3$	a	2.1063×10^{-8}	-5.6064×10^{-5}	8.8198
	c	-5.0656×10^{-8}	3.3971×10^{-4}	22.873
	V	3.8497×10^{-6}	3.2512×10^{-3}	1540.9
$AgTiZr(PO_4)_3$	a	2.7532×10^{-8}	-4.8276×10^{-5}	8.6362
	c	-2.0460×10^{-8}	2.9096×10^{-4}	22.479
	V	8.2513×10^{-6}	2.4518×10^{-3}	1493.9
$AgTi_{1.5}Zr_{0.5}(PO_4)_3$	a	2.8212×10^{-8}	-4.4201×10^{-5}	8.5560
	c	-1.9091×10^{-8}	2.8299×10^{-4}	22.296
	V	8.0881×10^{-6}	3.2809×10^{-3}	1413.3

Table 5.3: Experimentally determined CTEs for $AgZr_2(PO_4)_3$ ($\times 10^{-6}$ $^oC^{-1}$)

Temperature (^{o}C)	α_a	α_c	α_V	α_L[a]
25	-6.24	14.74	2.23	0.74
100	-5.88	14.39	2.61	0.87
200	-5.41	13.93	3.11	1.04
300	-4.93	13.47	3.61	1.20
400	-4.46	13.01	4.10	1.37
500	-3.98	12.55	4.60	1.53
600	-3.50	12.10	5.10	1.70
700	-3.02	11.64	5.59	1.86
800	-2.54	11.19	6.09	2.03
900	-2.07	10.74	6.58	2.19

[a] $\alpha_L = 1/3\ \alpha_V$

Table 5.4: Experimentally determined CTEs for $Ag[TiZr](PO_4)_3$ ($\times 10^{-6}$ $^oC^{-1}$)

Temperature (^{o}C)	α_a	α_c	α_V	α_L[a]
25	-5.43	12.90	1.92	0.64
100	-4.96	12.89	2.75	0.92
200	-4.32	12.87	3.85	1.28
300	-3.68	12.85	4.95	1.65
400	-3.04	12.84	6.05	2.02
500	-2.41	12.82	7.15	2.38
600	-1.77	12.81	8.25	2.75
700	-1.13	12.79	9.34	3.11
800	-0.49	12.78	10.43	3.48
900	0.15	12.76	11.51	3.84

[a] $\alpha_L = 1/3\ \alpha_V$

Table 5.5: Experimentally determined CTEs for $Ag[Ti_{1.5}Zr_{0.5}](PO_4)_3$ (x 10^{-6} $^oC^{-1}$)

Temperature (^oC)	α_a	α_c	α_V	α_L [a]
25	-5.00	12.65	2.61	0.87
100	-4.51	12.51	3.47	1.15
200	-3.85	12.32	4.61	1.54
300	-3.19	12.13	5.75	1.92
400	-2.53	11.95	6.88	2.29
500	-1.87	11.76	8.02	2.67
600	-1.21	11.58	9.16	3.05
700	-0.55	11.40	10.28	3.43
800	0.11	11.21	11.41	3.80
900	0.77	11.03	12.54	4.18

[a] $\alpha_L = 1/3\ \alpha_V$

5.3 Conclusions

High temperature powder X-ray diffraction measurements did not show any differences in the crystal structures of $AgTiZr(PO_4)_3$ and $AgTi_{1.5}Zr_{0.5}(PO_4)_3$ at high temperature. Bottleneck size in the $AgTi_2(PO_4)_3$ structure is the smallest and it does not allow an open pathway for the ion exchange. As the smaller ion, Ti^{4+}, is substituted by the bigger one, Zr^{4+}, the size of the bottlenecks around the Zr^{4+} increases. Apparently there is a threshold solid solution composition, $x > 1$, where a pathway exists through the material for ion exchange.

$AgZr_2(PO_4)_3$, $AgTiZr(PO_4)_3$ and $AgTi_{1.5}Zr_{0.5}(PO_4)_3$ are positive thermal expansion materials with a high degree of anisotropy; cell parameter a contracts and c expands upon heating. Comparison of the coefficients of thermal expansion shows that the thermal expansion anisotropy decreases (the difference between α_a and α_c) as the bigger ion, Zr^{4+}, is substituted by the smaller one, Ti^{4+} (Table 5.6).

Table 5.6: Experimentally determined average CTEs (x 10^{-6} $^{o}C^{-1}$) between 25 ^{o}C and 900 ^{o}C

Material	α_a	α_c
$AgZr_2(PO_4)_3$	-4.15	12.8
$Ag[TiZr](PO_4)_3$	-2.61	12.1
$Ag[Ti_{1.5}Zr_{0.5}](PO_4)_3$	-2.12	11.9

CHAPTER 6

COMPARISON OF THERMOPHYSICAL PROPERTIES FOR $MZr_2(PO_4)_3$ (M=Ag, Ga, In, Li, Na, K, Rb, Cs)

6.1 Comparison of the Ionic Radii

Substitution of the M(I) site with a bigger alkali metal increases the unit cell parameters and volume. If it is assumed that the trend is linear then the unit cell parameters and volume as a function of ionic radius (R) can be fitted to a linear equation (3). The unit cell parameters of Ag, Ga and In can be inserted into the equations, and the ionic radius in a six coordinate oxygen environment can be calculated (Figure 5.5 and 5.6).

(3) $p = p_1 R + p_0$

Table 6.1: Ionic radii, unit cell parameters and volume of alkaline metals and Ag, Ga and In.

Element	Univalent Ionic Radius[1]	a (Å)[a]	c (Å)[a]	v (Å)[a]
Li	0.59	8.875	22.277	1518.60
Na	1.02	8.810	22.734	1528.20
K	1.38	8.717	23.899	1572.00
Rb	1.49	8.659	24.478	1589.98
Cs	1.7	8.621	24.865	1600.55
Ag	1.15	8.818	22.881	1540.92
Ga	-	8.723	23.880	1573.37
In	-	8.671	24.345	1585.20

[a] Lattice constants for $MZr_2(PO_4)_3$ (M = Li, Na, K, Rb and Cs) are taken from Tylor[2]. Lattice constants for $GaZr_2(PO_4)_3$, $InZr_2(PO_4)_3$ and $AgZr_2(PO_4)_3$ were determined from data collected at the HTML.

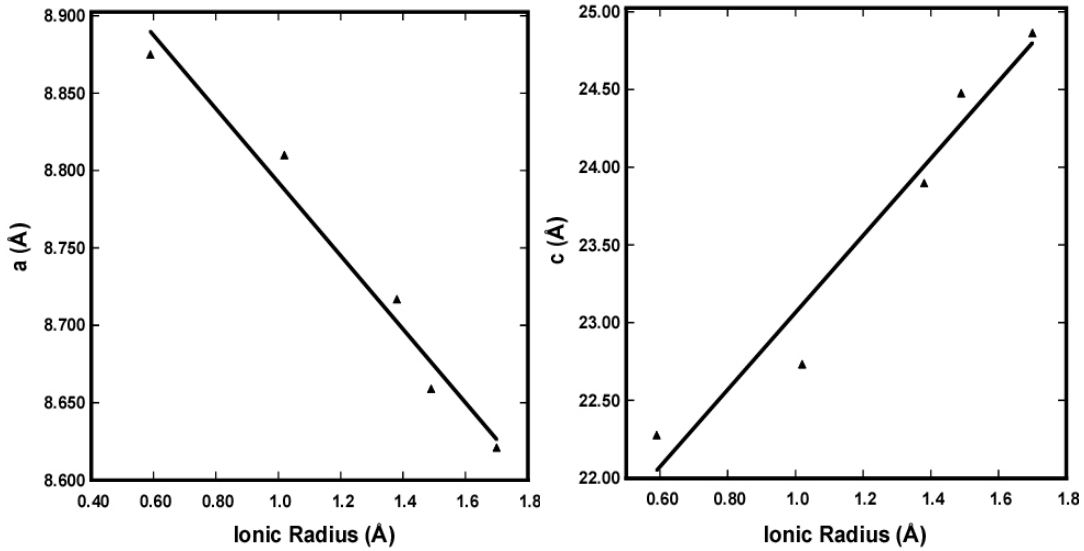

Figure 6.1: Unit cell parameters, a (Left) and c (Right), as a function of radius. Radii are taken from Shannon[1], unit cell parameters of $MZr_2(PO_4)_3$ (M = Li, Na, K, Rb and Cs) are taken from Taylor[2].

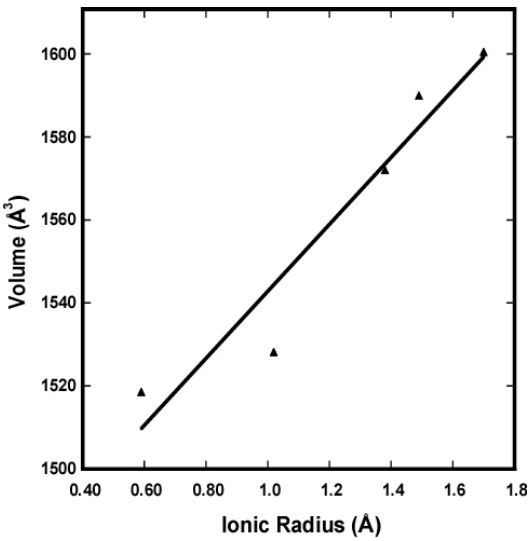

Figure 6.2: Unit cell volume as a function of radius. Radii are taken from Shannon[1], unit cell volume of $MZr_2(PO_4)_3$ (M = Li, Na, K, Rb and Cs) are taken from Taylor[2].

Table 6.2: Parameters extracted from the linear equations.

Axis	p_1	p_0
a	- 0.23731	9.0297
c	2.4783	20.587
V	80.798	1462

The calculated radius of Ag(I), using the linear equations, is very different from the reported one[1] suggesting that Ag(I) does not behave like an alkali metal in the M(I) site. If Ga(I) and In(I) behave as alkali metals, then the ionic radii of Ga(I) and In(I) would be 1.29-1.33 and 1.51-1.52, respectively.

Table 6.3: Ionic radii calculated using the fitted equations.

Element	Ionic Radius[1]	Ionic Radius[a]	Ionic Radius[b]
Li	0.59	0.65	0.68
Na	1.02	0.93	0.87
K	1.38	1.32	1.34
Rb	1.49	1.56	1.57
Cs	1.7	1.72	1.73
Ag	1.15	0.89	0.93
Ga	-	1.29	1.33
In	-	1.51	1.52

[a]Calculated using the equation for a.
[b]Calculated using the equation for c.

6.2 Comparison of the Thermal Expansion Behavior

The thermal expansion behavior of $AgZr_2(PO_4)_3$, $GaZr_2(PO_4)_3$ and $InZr_2(PO_4)_3$ is anisotropic; the a parameter decreases while the c parameter increases. The behavior of $GaZr_2(PO_4)_3$ and $AgZr_2(PO_4)_3$ are very similar to the behaviors of $KZr_2(PO_4)_3$ and $NaZr_2(PO_4)_3$, respectively (Figure 5.7 and 5.8).

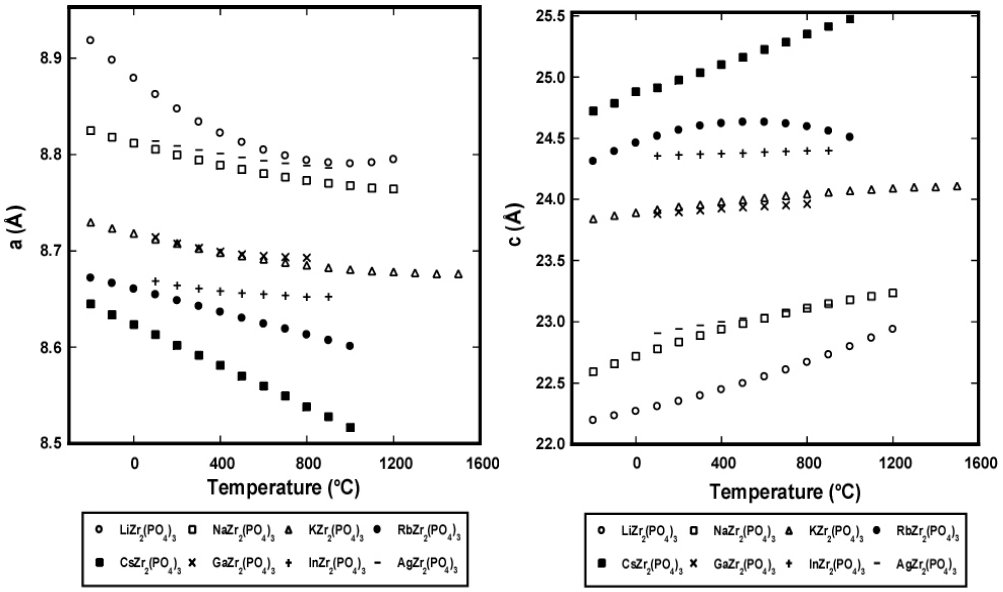

Figure 6.3: The cell parameters, a (Left) and c (Right), as a function of temperature. $MZr_2(PO_4)_3$ (M = Li, Na, K, Rb and Cs) are taken from Taylor.[2] $InZr_2(PO_4)_3$ and $AgZr_2(PO_4)_3$ cell constants were derived from data collected at HTML and $GaZr_2(PO_4)_3$ data were collected at APS.

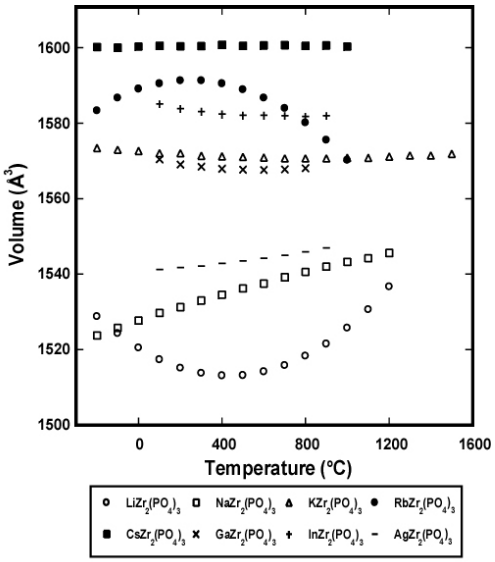

Figure 6.4: Unit cell volume as a function of temperature. $MZr_2(PO_4)_3$ (M = Li, Na, K, Rb and Cs) are taken from Taylor.[2] $InZr_2(PO_4)_3$ and $AgZr_2(PO_4)_3$ cell constants were derived from data collected at HTML and $GaZr_2(PO_4)_3$ data were collected at APS.

6.3 References

1. Shannon, R. D.; Prewitt, C. T., Effective Ionic Radii in Oxides and Fluorides. *Acta Crystallograohica Section B* **1969,** 25, 925-946.

2. Taylor, D., Thermal Expansion Data: XIV Complex Oxides with the Sodalite and Nasicon Framework Structures. *British Ceramic Transactions and Journal* **1991,** 90, 64-69.